INFLUENCE OF PRE-ERUPTIVE DEGASSING AND CRYSTALLIZATION ON THE DEPOSITS OF LATERALLY DIRECTED VOLCANIC EXPLOSIONS

A THESIS SUBMITTED TO THE GRADUATE DIVISION OF THE
UNIVERSITY OF HAWAI'I IN PARTIAL FULFILLMENT
OF THE REQUIREMENTS FOR THE DEGREE OF

MASTER OF SCIENCE

IN

GEOLOGY AND GEOPHYSICS

DECEMBER 2009

By

Owen Kelly Neill

Thesis Committee:

Julia E. Hammer, Chairperson
Bruce F. Houghton
John M. Sinton

We certify that we have read this thesis and that, in our opinion, it is satisfactory in scope and quality as a thesis for the degree of Master of Science in Geology and Geophysics.

Thesis Committee

_____

Chairperson

_____

_____

This thesis is dedicated to the men and women of the 2008 PIRE-Kamchatka team, with great gratitude and respect.

If the conquest of a great peak brings moments of exultation and bliss, which in the monotonous, materialistic existence of modern times nothing else can approach, it also presents great dangers. It is not the goal of grand alpinisme to face peril, but it is one of the tests one must undergo to deserve the joy of rising for an instant above the state of crawling grubs. On this proud and beautiful mountain we have lived hours of fraternal, warm and exalting nobility. Here for a few days we have ceased to be slaves and have really been men. It is hard to return to servitude."
- Lionel Terray.

"Bezy style."
- Anonymous.

ACKNOWLEDGEMENTS

I would like to thank my advisor, Julia Hammer, for her seemingly endless patience and for sharing the staggering depths of her knowledge and creativity with me. I am very grateful to my collaborators, Pavel Izbekov (Univ. Alaska – Fairbanks) – who contributed formative ideas and extraordinary effort into seeing this project through – Alexander and Marina Belousov(a) (IVS, Petropavlovsk-Kamchatsky), Amanda Clarke (Arizona State U.) and Barry Voight (Penn. State U.), all of whom have devoted much time and energy to this work. My committee members, Bruce Houghton and John Sinton, have not only provided helpful comments on this thesis but have been outstanding educators in both the field and classroom. I especially thank the 2008 PIRE-Kamchatka team, the staff of IVS and the pilots of Камчатские Авиалинии for invaluable help in fieldwork and sample collection; Jessica Larsen, Rainier Newbury, Ken Severin, and the UAF Experimental Petrology group for the use of their lab spaces; and Eric Hellebrand for copious help with the microprobe and XRF. Torsten Vennemann (U. Lausanne) performed the manometry analyses presented herein. Leslie Almberg (UAF), Kim Genareau (ASU), Malcolm Rutherford (Brown U.), Jill Shipman (UAF), and Wendy Stovall provided useful samples and images. Janet Becker, Julie Bowles, Carrie Brugger, Sarah Fagents, Chuck Fraley, Mike Garcia, Anette von der Handt, Gary Huss, Megadeth, Gordon Moore (ASU), Kazuhide Nagashima, Ken Rubin, Tom Shea and Lisa Tatsumi-Petrochilos provided analytical assistance and insightful discussions. Finally, I thank the grad students of GG for their friendship, and my parents for their love and support. This work was funded by Amherst College, the National Science Foundation Project for International Research and Education – Kamchatka, and by NSF CAREER Award EAR04-49888 to Julia Hammer.

ABSTRACT

The progressive growth of a silicic volcanic cryptodome can lead to increasing instability in the overlying volcanic edifice, flank failure, possibly accompanied by a destructive, laterally-directed explosion, or directed blast. Two strikingly similar examples of this are found in the 18 May 1980 eruption of Mount St. Helens, Washington, USA, and the 30 March 1956 eruption of Bezymianny Volcano, Kamchatka, Russia. In these cases, flank failure led to near-instantaneous cryptodome decompression and fragmentation, which produced catastrophic, laterally-directed blasts. These blasts, in turn, produced juvenile material with bimodal density/vesicularity distributions that indicate non-uniform vesiculation during fragmentation. In blast material sampled from both Mount St. Helens and Bezymianny, pre-blast crystallization led to a pronounced disparity in crystal content between low vesicularity (up to 100 vol% crystals) and high-vesicularity material (70-75 vol% crystals). Bulk-rock H_2O and ∂D measurements show that blast material experienced progressive open-system outgassing prior to eruption, and that clasts with higher crystallinity had outgassed more than less crystalline material. Progressive pre-blast outgassing of cryptodome material is also reflected in the compositions of the constituent minerals and glasses, suggesting low-pressure, degassing-driven groundmass crystallization prior to flank failure and lateral blast. The crystallinity disparity suggests that during the directed blast, some of the blast material was prevented from expanding during fragmentation by extensive degassing-induced pre-blast groundmass crystallization. An inferred rheological control on vesiculation compounded the effects of non-uniform volatile distribution within the cryptodome (Hoblitt and Harmon 1993, Alidibirov et al. 1997) in creating bimodal pyroclast densities.

TABLE OF CONTENTS

LIST OF TABLES

LIST OF FIGURES

1. INTRODUCTION

The similarities between the 30 March 1956 eruption of Bezymianny Volcano (abbreviated hereafter as BZ), in Kamchatka, Russia, and the 18 May 1980 eruption of Mount St. Helens (abbreviated as MSH) in Washington, USA have been noted or investigated by numerous authors (Lipman et al. 1981a, Cashman and Taggart 1983, Bogoyavlenskaya et al. 1985, Crandall and Hoblitt 1986, Belousov 1996, Belousov et al. 2007). Both eruptions followed a similar sequence of events – months of cryptodome emplacement prior to explosion; edifice deformation and phreatic-phreatomagmatic explosions; flank failure; a directed lateral volcanic blast caused by the fragmentation of the cryptodome; a climactic Plinian eruption; and post-eruptive dome growth within the eruptive crater. This study (a.) examines and compares volatile distributions and crystallization conditions within the cryptodomes at BZ and MSH prior to the lateral blasts, and (b.) investigates the effects of these conditions on the density distributions of pyroclastic deposits produced by these blasts. Differences in the density and vesicularity – which is linearly correlated with density (Houghton and Wilson 1989) – distributions of a pyroclastic deposit result from contrasting ascent and fragmentation processes (e.g. Gurioli et al. 2005, Adams et al. 2006); investigating the parameters that control them, such as pre-explosive outgassing and crystallization, can shed light on the physical state of the magma when the cryptodomes fragment at the onset of the directed blasts.

1.1 Description of Blast-Related Eruptive Events at BZ and MSH

Detailed descriptions of the awakening, deformation and cryptodome emplacement, debris avalanche, directed lateral blast, climactic Plinian eruption and post-

eruptive cryptodome-building associated with the1956 eruption of BZ have been published extensively elsewhere (Gorshkov 1959, Gorshkov 1963, Gorshkov and Bogoyavlenskaya 1965, Alidibirov et al. 1990a,1990b, Braitseva et al. 1991, Belousov 1996, Belousov and Belousova 1998, Belousov et al. 2007). To summarize (after Gorshkov and Bogoyavlenskaya 1965), on 29 September 1955, after ~1000 years of quiescence (Braitseva et al. 1991), seismic activity was recorded at an estimated depth of 50 km beneath BZ. Phreatomagmatic explosions and increasing seismicity began around 22 October and peaked around 16-17 November; cryptodome growth also began around this time, with the associated deformation of the southeast slope of the edifice reaching or exceeding 100 m (Gorshkov 1959). During the period of November 1955 – March 1956, seismicity and Vulcanian explosions waned in intensity, though the cryptodome continued to grow. Finally, on 28 March, activity increased, with ash fall reported in the nearby town of Klyuchi; finally, on 30 March 1956, the catastrophic eruption began when the deformation of the edifice critically destabilized it, causing a debris avalanche of 0.5 km^3 (Belousov and Bogoyavlenskaya 1988), followed within seconds by a directly lateral blast that covered an area of 500 km^2 with 0.2 km^3 of material (Belousov 1996). The explosion reduced the height of BZ by ~200 m, leaving a crater of an area of nearly 5 km^2 (Belousov et al. 2007). A large, open-conduit eruption dominated by pumiceous andesite-rich pyroclastic flows, as well as an eruptive column ~34-38 km in height followed (Belousov 1996). Dome growth within the crater began immediately after the eruption, and has continued to the present time, interspersed with intermittent, periodic explosions (Bogoyavlenskaya and Kirsanov 1981, Alidibirov et al. 1990a, Belousov 1996).

Detailed descriptions of the events at Mount St. Helens on and leading up to 18 May, 1980 have been published in even greater detail than at BZ (Lipman and Mullineaux 1981 and references therein). To summarize, activity commenced with a shallow earthquake swarm on 20 March, 1980, followed by phreatic explosions beginning on 27 March (Moore and Albee 1981). Prior to 20 March, the most recent eruptive activity had been the emplacement of the Goat Rocks dome ~150 years prior, while the most recent explosive activity had been ~400 years earlier (Mullineaux and Crandall 1981). 27 March also marked the beginning of cryptodome-growth-associated edifice bulging, which continued at a rate of ~1.5-2.5 m/day and reached a maximum of 150m prior to eruption (Lipman et al. 1981a). Phreatic explosions continued from 27 March – 14 May, with a hiatus from 22 April – 7 May; edifice bulging and deformation, the result of cryptodome emplacement, was continuous throughout (Christiansen and Peterson 1981). The catastrophic landslide of 18 May contained ~2.5 km^3 of material (Voight et al. 1981), and the following directed blast distributed ~0.11 km^3 of material of a 600 km^2 area (Hoblitt and Harmon 1993). A large Plinian eruption followed, producing pyroclastic density currents and a 20 km ash column (Christiansen and Peterson 1981). Post-climactic dome, interspersed with small explosive eruptions, growth continued until 1986, and re-activated from 2004-2008 (Christiansen and Peterson 1981, Moore et al. 1981, Scott et al. 2008).

1.2 Mechanisms of Directed Volcanic Blasts

The term "directed blast," first coined by Gorshkov (1959) in describing the 1956 BZ eruption, refers to a large, highly destructive, laterally directed volcanic explosion or

series of explosions (Hoblitt 2000), resulting in a pyroclastic density current, often associated with flank failure. While other terms such as “blast flow” (Kieffer 1981a), “blast surge (Fisher 1990, Belousov 1996), “pyroclastic density flow” (Hoblitt 2000) and “pyroclastic density current” (Druitt and Kokelaar 2002) have been applied to such phenomena, “directed volcanic blast,” or “blast,” is adopted here after Belousov et al. (2007). Directed volcanic blasts are inferred to be the result of the growth, vesiculation and fragmentation of a shallowly-emplaced, gas-overpressured magma body, the emplacement of which destabilizes the volcanic edifice and leads to the eventual flank collapse (Gorshkov 1959, 1963, Voight et al. 1981, Lipman et al. 1981a, Belousov and Bogoyavlenskaya 1988). The sector collapse removes a significant amount of overburden material from the volcanic edifice, and the resulting loss of confining pressure allows rapid bubble growth and fragmentation driven by the release of the gas pressure (Hoblitt et al. 1981, Alidibirov and Dingwell 1996, Voight and Elsworth 2000). Bubble growth is driven in large part by pressure stored in bubbles from volatiles that have formed by magmatic degassing during ascent and emplacement (Alidibirov 1995, Navon et al. 1998). Syn-eruptive diffusion of volatiles into bubbles may also occur, as indicated by the presence of breadcrust bombs with low (~1200 kg/m^3) internal densities (Hoblitt et al. 1981, Alidibirov et al. 1997). While flank failure may still trigger an eruption, a directed blast cannot be generated without a volatile-rich, shallow magma body (Figure 1). For example, the1964 eruption of Shiveluch in Kamchatka, and the 1933 eruption of Harimkotan, in the Kurile Islands, both included flank collapses that were followed by Plinian eruptions with no directed blast in between (Belousov et al. 2007). Other directed blasts have been reported at Soufriere Hills Volcano, Montserrat (Ritchie et al. 2002) and

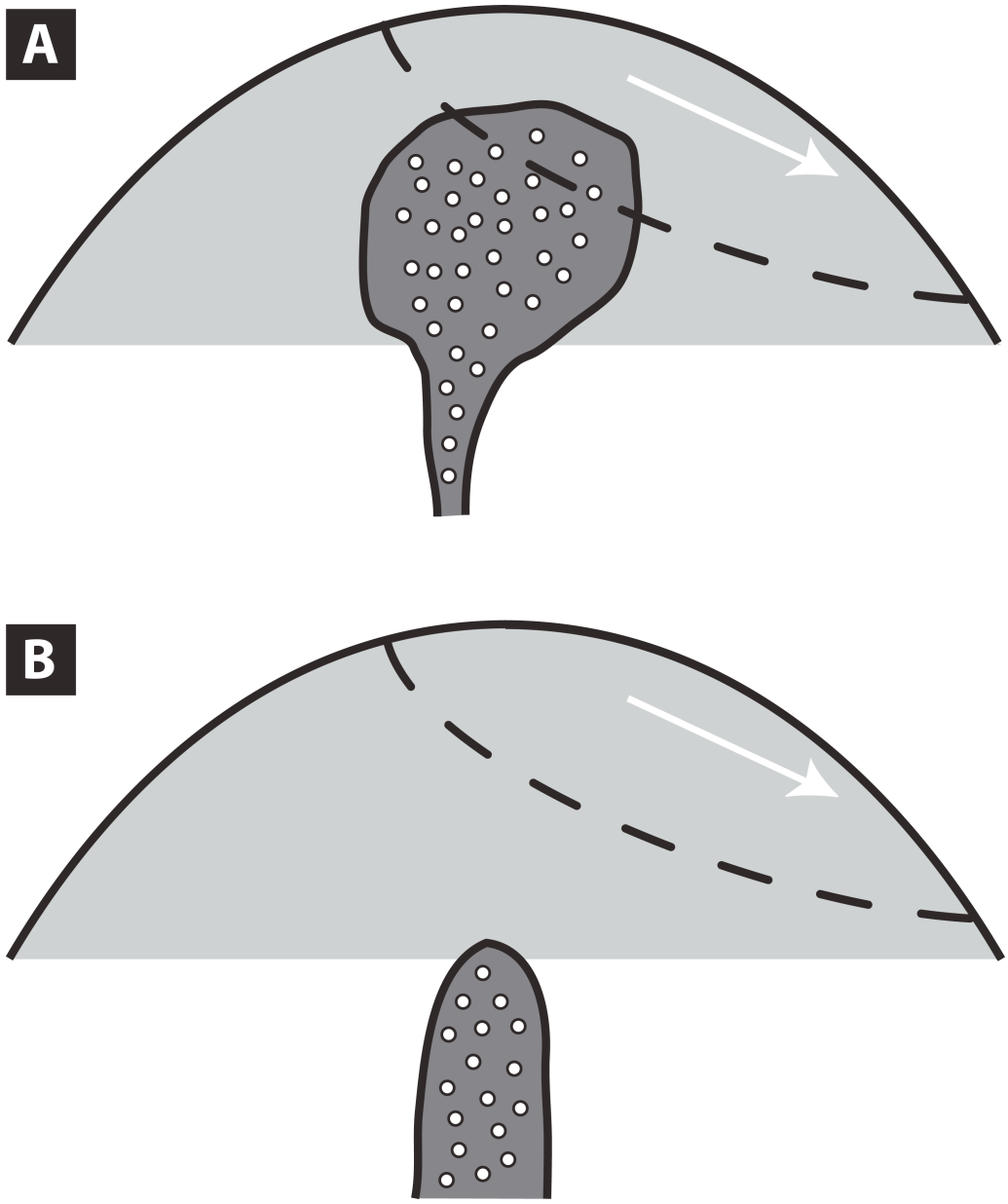

*Figure 1: Schematic representations of volcanic edifice collapse that is A. likely and B. unlikely to trigger a directed blast. When the surface of the debris avalanche scarp (dashed lines) intersects a volatile-charged magma body (dark grey) within the volcanic edifice (**A.**), as at MSH and BZ (Belousov et al. 2007), the instantaneous decompression of the cryptodome leads to its vesiculation, fragmentation and a directed blast. When the magma body is not emplaced high enough in the edifice to be intersected by the avalanche scarp (**B.**), as was the case at Harimkotan in 1933 and Shiveluch in 1964, no blast is triggered (Belousov et al. 2007). Arrows indicate direction of flank collapse. Figures based on Belousov et al. (2007).*

Augustine, Alaska (Siebert et al. 1995). Comparative studies of the BZ and MSH blasts, as well as with other similar eruptions (e.g. Bogoyavlenskaya et al. 1985, Belousov et al. 2007) can help determine which features of directed blasts are ubiquitous, and which are unique to individual eruptions.

1.3 Density and Vesicularity of Blast Pyroclasts

The range in vesicularity among clasts within the BZ and MSH blast deposits confers a noticeably darker coloration to dense clasts. As such, dense clasts were initially dismissed as accidental material at MSH, until Hoblitt and Harmon (1993) demonstrated that they were indeed juvenile, and that while the MSH deposit showed a continuous spectrum with respect density and vesicularity, the frequencies of dense and vesicular clasts were bimodally distributed (Figure 2). This color disparity led Hoblitt and Harmon (1993) to divide the two density modes of the blast dacite at MSH into "black" and "grey" categories, with black corresponding to the dense clasts and grey the more vesicular, with 2000 kg/m^3 accepted as the cutoff between black and grey. Blast deposits at BZ also show a bimodal frequency distribution (Figure 2, Belousov 1996, Belousov et al. 2007), though, unlike at MSH, black clasts dominate, accounting for ~65 vol% of the deposit, as opposed to only 28 vol% at MSH (Hoblitt and Harmon 1993, Belousov et al. 2007). The same cutoff value and black/grey terminology are used herein to differentiate the dense and vesicular material from both MSH and BZ blast deposits, though it should be noted that differentiating blast material as "black" and "grey" refers to a difference in clast *density*, and does not necessarily reflect the *color* of the material in question.

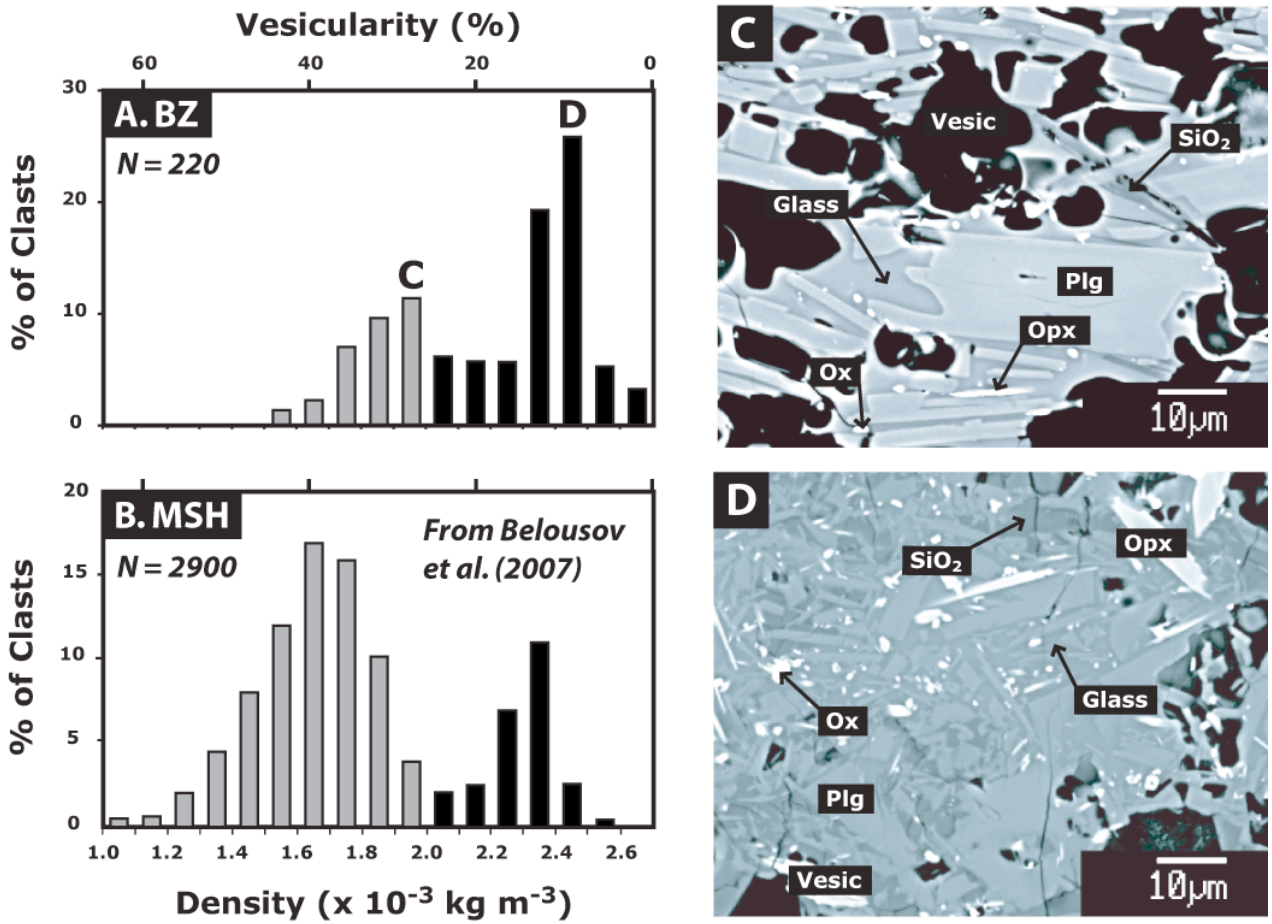

Figure 2: A,B: Density distributions for BZ and MSH (Belousov et al. 2007) respectively. N = the number of clasts used to create the histogram. Grey and black material is distinguished at 2000 kg/m^3 after Hoblitt and Harmon (1993), and colored appropriately. C,D: Backscatter electron images of BZ grey (C) and black (D) material, taken from the fractions indicated in A, showing the qualitative differences in vesicularity and crystal content between the two density modes. Phases abbreviations: Plg = Plagioclase, OPX = Orthopyroxene, SiO_2 = Quartz, Ox = Fe-Ti Oxides, Vesic = Vesicle.

1.4 Volatile Loss, Crystallization and Fragmentation of Volcanic Cryptodomes

Silicic dome lavas are outgassed relative to magma in crustal storage reservoirs, primarily because of the dependence of volatile solubility on confining pressure (e.g. Hoblitt and Harmon 1993, Moore et al. 1998). H_2O loss increases magma liquidus temperature, thereby creating an effective undercooling that drives crystallization (Geschwind and Rutherford 1995). Such degassing-driven crystallization has been inferred as the mechanism of crystallization at silicic domes such as the 1980-1986 domes at MSH (Cashman 1992, Blundy and Cashman 2001), Unzen (Nakada and Motomura 1999) and Merapi (Hammer et al. 2000).

Both outgassing and crystallization can exert control on how bubbles within a melt expand during fragmentation, and therefore affect the post-eruptive densities and vesicularities of pyroclasts. Hoblitt and Harmon (1993) concluded that heterogeneous volatile loss from MSH cryptodome material during magma ascent and storage within the cryptodome was the cause of the bimodal clast density distributions, whereby the magma destined to become the black material had lost sufficient volatiles prior to the blast to prevent syn-blast vesiculation. This conclusion was supported by the study of Alidibirov et al. (1997), who suggested that the heterogeneous outgassing prior to fragmentation demonstrated by Hoblitt and Harmon (1993) led to a heterogeneous distribution of bubbles within the MSH cryptodome prior to fragmentation, and that this variation in vesicularity was preserved upon fragmentation; material that remained dense was volatile-poor prior to the blast, and thus experienced no syn-blast bubble growth, while material that expanded experienced sufficient bubble expansion to fragment the cryptodome. Crystallization, and specifically changes in crystal content, can also exert

control on vesiculation. Klug and Cashman (1994) demonstrated that increased pre-fragmentation microlite contents restricted bubble growth in MSH grey pumice to a degree not seen in the relatively crystal-poor white pumice. While the high groundmass crystallinity and pervasive cracking of both BZ and MSH blast material eliminates a comprehensive study of vesicle textures to understand syn-fragmentation vesiculation processes (e.g. Adams et al. 2006), the solid phases in the blast deposits remain pristine enough to investigate volatile distribution and crystallization conditions within the BZ cryptodome, and compare them to both new and previously published studies of these conditions at MSH. Therefore, the goals for this study are as follows: To compare the pre-blast outgassing at BZ to the well-established models for MSH; to investigate the effects of degassing and outgassing on the bulk and groundmass crystallinity and phase compositions at both BZ and MSH; to comment on the effects of pre-blast outgassing and crystallization on bubble expansion during fragmentation, in light of existing models (e.g. Hoblitt and Harmon 1993); and to investigate the possible effects that outgassing and crystallization have on the post-eruptive density distributions of directed blast deposits.

2. METHODS

2.1 Sampling and Density/Vesicularity Measurements

BZ directed blast material was sampled in the summer of 2008 from two locations to the southwest of Bezymianny volcano (Figure 3). In order to obtain at least 100 clasts of juvenile material at each location, ~110 clasts were sampled at each location. Density

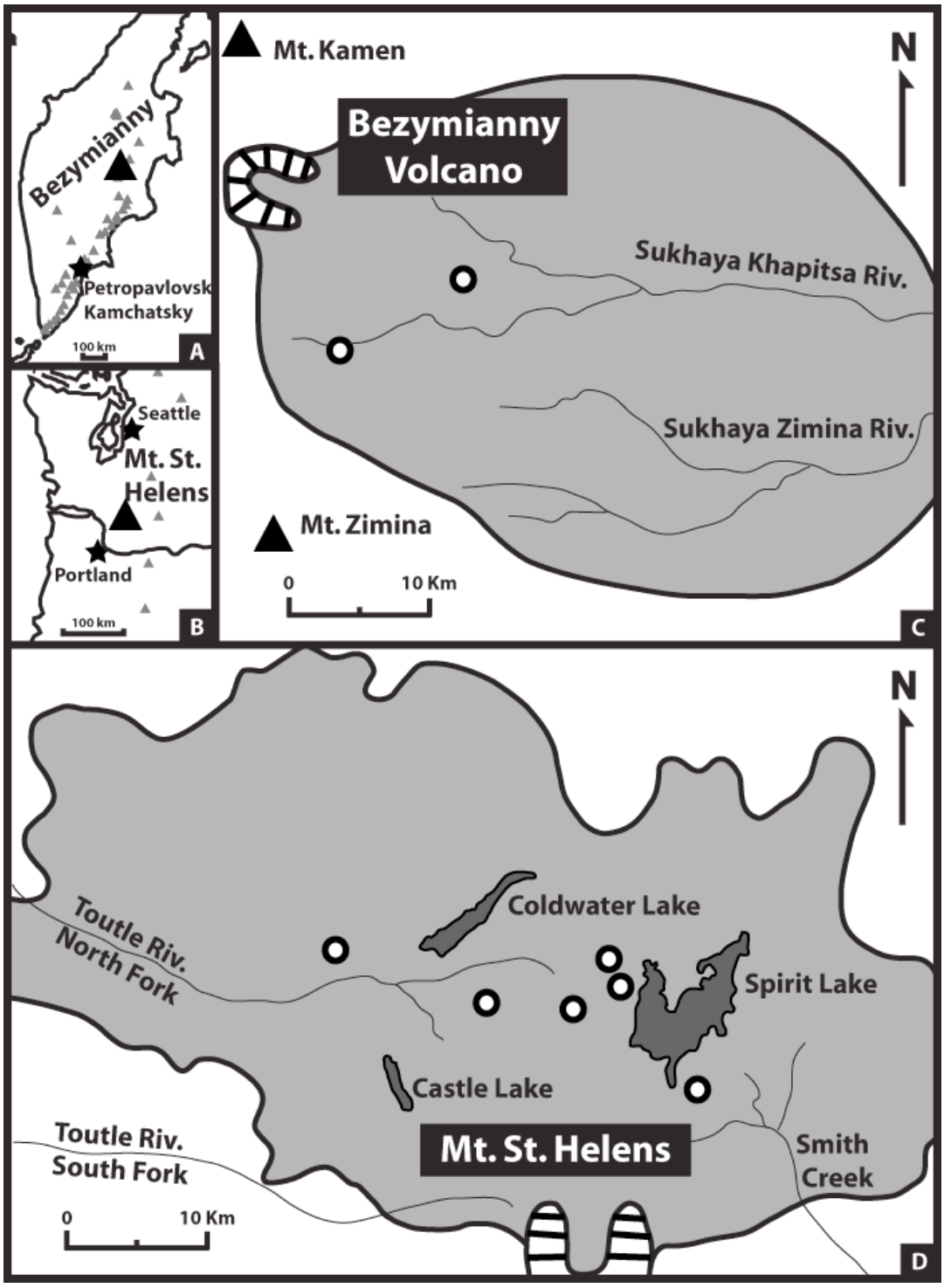

*Figure 3: **A**,**B**: General location maps for BZ and MSH volcanoes, respecctively. Grey triangles represent other Holocene volcanoes from the same respective arc systems. **C**,**D.** Locations of sample sites with selected local landmarks at BZ and MSH, respectively. Black-bordered circles represent sample locations. Light grey shaded areas represent the distribution of directed blast material at BZ (after Belousov 1996) and MSH (after Hoblitt et al. 1981).*

and vesicularity of these clasts were calculated using the method of Houghton and Wilson (1989), using silicone spray as a waterproofing medium and a dense-rock equivalent value of 2700 kg/m^3 for both MSH and BZ (Hoblitt and Harmon 1993, Belousov et al. 2007). Seven MSH clasts were taken from the sample set of Belousov et al. (2007, locations shown in Figure 3). At both MSH and BZ, only juvenile material was sampled; accidental clasts and clasts with obvious oxidation or alteration were discarded.

Clasts from each sample suite was chosen for bulk H_2O analysis, representing modal, minimum, maximum and intermediate density values, determined from each density distribution (Figure 2). Clasts were also selected for standard petrographic analysis of phase proportions and compositional analysis of glass and feldspar.

2.2 Modal Analysis

Phase proportions were determined through point counting of thin sections obtained from the clasts selected as above, as well as slides generously provided by Dr. W. K. Stovall. Trace phases apatite and K-feldspar (identified using X-ray mapping of both MSH and BZ groundmass) were ignored in modal analysis. Proportions of groundmass phases were obtained using 1500X-magnification backscatter electron (BSE) images using JMicroVision 1.2.7 software. BSE images were acquired using the JEOL 5900LV scanning electron microscope (SEM) at the University of Hawaii – Manoa. Ten images were collected per slide, for a total of 2200 groundmass points per slide. 1500X magnification was necessary to effectively distinguish fine-scale boundaries between groundmass phases, especially in the most crystalline material. Phenocryst proportions were obtained by point counting thin sections with a petrographic microscope with a

mechanical stage. As with the groundmass, 2200 points were counted at the phenocryst scale for a total of 4400 points counted per slide, leading to an average 2-σ uncertainty of less than ±1 vol% absolute (van der Plas and Tobi 1965). As the rocks have no discernable fabric, the area and volume fractions of phases were assumed to be identical (DeHoff and Rhines 1968). Weight fractions of each phase were calculated using the area fractions and published densities of crystal phases (Deer et al.1992). Glass density was calculated from glass compositions, obtained by electron microprobe (see below), using the model of Lange and Carmichael (1990).

2.3 Bulk Rock Chemistry

Four grey and four black andesite clasts from the BZ blast were measured for bulk chemistry by x-ray fluorescence (XRF); bulk chemistry of MSH blast material is published elsewhere (Hoblitt and Harmon 1993). Major, minor and trace element compositions were measured using a Siemens 303AS XRF spectrometry system with a Rh-target, end-window x-ray tube. Clasts were lightly crushed, inspected by binocular microscope to avoid including altered material, and then crushed to fine powder by hand. Powders were used to create fused disks, analyzed for major and minor elements using methods similar to Norrish and Hutton (1997), and pressed pellets, analyzed for trace elements, using background, interference and matrix correction schemes similar to those of Chappell (1992).

2.4 Electron Microprobe Analysis

Samples were chosen for microprobe analyses from across a range of densities in order to evaluate differences in phase chemistry among clasts of differing bulk density and crystallinity. All analyses of phase compositions were performed on the JEOL JXA-8500F Field Emission Hyperprobe at the University of Hawaii – Manoa, using a 15 KeV electron beam and beam current of 10 μA (15 μA for plagioclase). Na- and K-loss as well as Si "grow in" (Morgan and London 1996) were corrected using Time-Dependant Intensity (TDI) corrections incorporated in ProbeForWindows software (Donovan et al. 2007), and by analyzing Si, Na and K first. Concentrations were obtained from raw counts using a ZAF intensity correction. Samples were chosen from across a range of densities in order to evaluate differences in phase chemistry among clasts of differing bulk density and crystallinity.

Glass analyses were performed using a 1 μm beam. Counting times were 30 seconds on-peak and 15 seconds off-peak for all elements. The number of analyses per slide and the small spot size used were dictated by the highly crystalline nature of the groundmass in both BZ and MSH material, particularly black material. However, while 1 μm is a smaller beam diameter than is commonly used for glass analyses, repeated analyses of control standards STG-72 (used by Self and King 1996) and VG-568 (USNM 72854, Jarosewich 2002) produced accurate and reproducible results using identical beam condition (see Table 1). Plagioclase analyses were performed on microlites using a 1-3μm beam, using Andesine AC 362 (composition published in Anderson and Hinthorne 1973) as a bench standard. The small size of the microlites restricted analyses to one per grain. Counting times were 30 and 15 seconds, on- and off-peak respectively. Amphibole

Table 1: Analyses of glass standards with 1-μm beam.

	STG-72			VG-568		
	Published	Analyzed	2- σ	Published	Analyzed	2- σ
n		37.00			13.00	
SiO_2	71.1	71.1	1.11	76.7	77.0	1.26
TiO_2	0.54	0.55	0.07	0.12	0.08	0.10
Al_2O_3	12.8	12.8	0.28	12.0	12.1	0.29
FeO_T	5.54	5.54	0.32	1.23	1.18	0.17
MnO	0.14	0.13	0.03	0.03	0.01	0.03
MgO	1.99	2.00	0.08	<0.1	0.03	0.02
CaO	2.95	2.95	0.14	0.50	0.49	0.05
Na_2O	1.66	1.66	0.56	3.75	3.63	0.46
K_2O	3.59	3.59	0.35	4.89	4.81	0.26
P_2O_5	0.08	0.08	0.04	0.01	0.01	0.02
Total	100.39	100.4		99.23	99.34	

phenocrysts were analyzed with a 1 μm beam, using Durango Apatite (USNM 104021, Jarosewich 2002) as an "unknown" bench standard for Cl and Arenal Hornblende (USNM 111356, Jarosewich 2002) as a control for all other elements. On- and off-peak counting times were as follows: 90/45 s for K, 40/20 s for Mn, 30/15 s for Ti and Na, and 20/10s for Si, Al, Fe, Mg, and Ca. Amphibole was only analyzed in clasts from the BZ density modes; MSH amphibole has been analyzed previously (Rutherford et al. 1985).

2.5 Bulk-Rock H_2O Measurement

Bulk H_2O contents were obtained through Karl Fischer Titration (KFT) at the University of Alaska - Fairbanks using a Mitsubishi coulometric moister meter, model CA-06, v. 4.2, coupled with VA-21 vaporizer. Mitsubishi Chemical Company reagents Aquamicron CXU and Aquamicron AX were used as the cathode and anode solutions, respectively. Clasts were crushed to ≤200 μm and pre-dried overnight at 110°C in a vacuum oven. 15-20 mg of powder were then heated in the VA-21 for 15 minutes at 150°C to drive off any remaining adsorbed H_2O, and heated again at 1000°C to release H_2O from hydrous phases. Desiccated N_2 gas carried the liberated H_2O into the titration cell; the reaction between H_2O and iodine, generated columetrically in the titration cell, allowed for quantitative H_2O measurement (Behrens 1995, Kato 1999). Raw analyses were corrected against frequent measurements of standard WW2 (Westrich 1987, 0.324 wt% H_2O); these measurements were also used to calculate analytical uncertainty.

1000°C does not completely release H_2O bound in glass (Behrens 1995, Behrens and Stuke 2003, Leschik et al. 2004) and hydrous mineral phases (meaning amphibole in the case of both MSH and BZ). Measurement of an amphibole separate from pumice clast

SH084, generously provided by Dr. M.J. Rutherford (see Rutherford et al. 1985 for description). by both manometry and KFT revealed that KFT releases ~25% of H_2O contained in amphibole. Behrens and Stuke (2003) showed that ~0.17±0.04 wt% H_2O is not released from glass during KFT. Therefore, corrections for unreleased H_2O are made based on the weight fractions of glass and amphibole in each clast. For MSH material, all 8 clasts analyzed for bulk H_2O by KFT were also analyzed by point counting, so the glass and amphibole contents and uncertainties are known directly. For BZ, only a portion of the clasts analyzed for bulk H_2O were also analyzed by point counting; consequently, phase proportions in the other clasts must be obtained by extrapolation. Although the glass content of BZ clasts increases with density, amphibole stays essentially constant at an average of ~7.9± 2.3 wt% (Figure 4). For clasts not analyzed by point counting, the average amphibole content is assumed, and glass content estimated based on density using the linear approximation shown in Figure 4, with a 2-σ uncertainty for glass content of ±4 wt%. Unreleased H_2O is accounted for using these phase proportions.

2.6 Manometry

The deuterium/hydrogen ratio of a volcanic rock can help to reveal its pre-eruptive degassing history (e.g. Taylor 1986). Amphibole H_2O content and bulk-rock hydrogen isotopic content of a subset of BZ blast clasts were obtained by manometry at the Université de Lausanne. Because of the difficulties of accurately measuring D/H ratios in samples with low bulk H_2O (<0.15-0.2 wt%, Dr. T.W. Venneman, pers. comm.) and possible kinetic effects on D/H partitioning at these low H_2O contents leading to anomalous deuterium enrichment (Anderson and Fink 1989), samples yielding <0.25

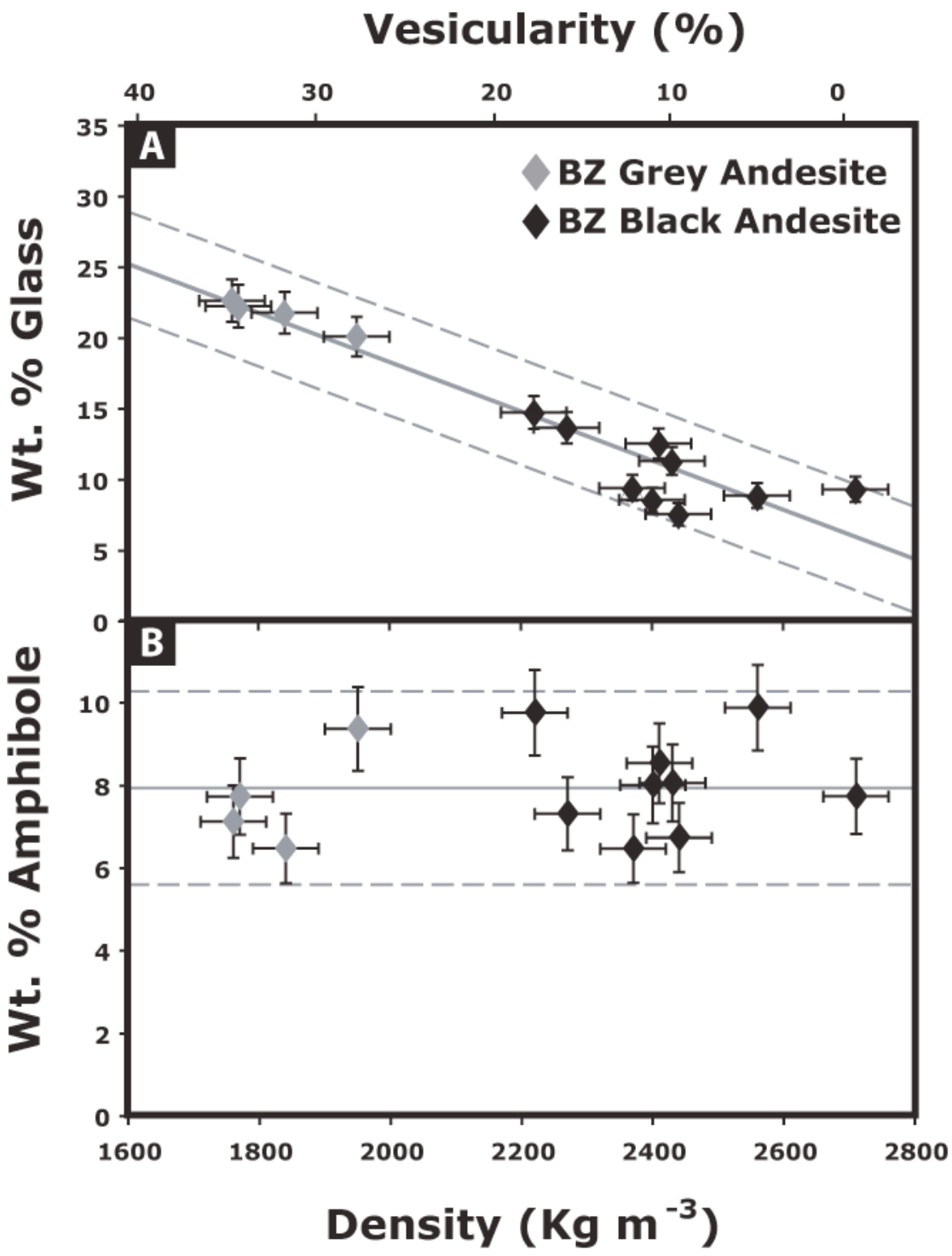

*Figure 4: Glass (**A**) and amphibole (**B**) contents, in wt. %, for BZ samples, measured by point counting on a vesicle-free basis (see text). Solid grey lines represents the linear approximation of glass content dependant on density in **A**, and the average amphibole content of BZ material in **B**. Dashed grey lines represent 2-σ uncertainty.*

wt% H_2O were not included in interpretations. Samples were analyzed with a TC-EA coupled to a DeltaPlus XL isotope ratio mass spectrometer (IRMS). 5-10 mg of powdered sample (≤120 μm) were dried at 150°C, then heated rapidly in flowing He gas to 1450°C, liberating H_2 from H_2O. The flowing He gas carried the liberated H_2 into the IRMS. Five BZ blast clasts, were analyzed for hydrogen isotopes using the method of Sharp et al. (2001); amphibole H_2O content was determined using the method of Vennemann and O'Neil (1993), on a separate from the MSH white pumice clast SH-084 (described by Rutherford et al. 1985).

3. RESULTS

3.1 Bulk Rock Compositions

Bulk rock compositions, obtained by X-ray fluorescence, are the same for black and grey BZ blast material (Table 2). As was the case at MSH (Lipman et al. 1981b, Hoblitt and Harmon 1993), BZ black and grey material are chemically indistinguishable not only from each other but from post-blast juvenile pumice produced during later phases of the climactic eruption (Belousov 1996, Table 3 of Ozerov et al. 1997), indicating that each of these components is derived from the same juvenile magma. Differences between them are thus interpreted as the result of post-formation crystallization and vesiculation processes – a finding that echoes Hoblitt and Harmon (1993) for MSH – rather than as the differences between separate magmas erupted simultaneously. Also the Losses on Ignition (LOI, Table 2) of grey material, though a decidedly imperfect way of estimating H_2O contents, are markedly higher than that of black material.

Table 2: Bulk XRF chemical analyses of BZ blast andesite. Oxides are in wt. % with all Fe as Fe_2O_3, trace elements in ppm.

Black/Grey	Grey	Grey	Grey	Grey	Black	Black	Black	Black
SiO_2	60.5	61.1	60.3	60.7	61.0	61.0	61.7	61.5
TiO2	0.63	0.61	0.59	0.59	0.62	0.58	0.60	0.56
Al_2O_3	18.4	18.3	17.8	17.5	18.3	18.6	18.2	18.9
Fe_2O_3*	6.77	6.68	6.46	6.48	6.82	6.55	6.64	6.27
MnO	0.15	0.15	0.14	0.14	0.15	0.14	0.15	0.14
MgO	2.73	2.50	2.75	2.71	2.65	2.38	2.41	2.21
CaO	6.91	6.65	6.54	6.30	6.68	6.75	6.54	6.76
Na_2O	3.08	3.09	3.60	3.50	3.11	3.08	3.09	3.20
K_2O	1.22	1.26	1.30	1.32	1.25	1.24	1.30	1.25
P_2O_5	0.18	0.18	0.18	0.18	0.18	0.19	0.20	0.19
Total	100.5	100.4	99.7	99.4	100.7	100.5	100.8	101.0
LOI	0.26	0.30	0.25	0.41	0.01	-0.04	0.11	-0.05
Sc	10	9	9	10	10	8	8	8
V	76	62	61	65	69	63	61	51
Mn	707	681	647	661	690	674	694	637
Co	8	7	8	7	8	7	7	7
Ni	6	5	9	6	8	4	6	6
Zn	72	71	66	66	71	71	73	66
Rb	24	25	27	27	25	25	26	25
Sr	354	355	354	340	353	365	344	379
Y	20	20	19	20	19	19	20	18
Zr	110	113	113	120	114	113	119	113
Ba	265	275	295	294	271	273	280	280
Pb	3	3	3	2	3	3	2	3

3.2 Phase Proportions

Perhaps the most striking observation to be drawn from the phase proportions (Table 3) is the strong correlation between density and groundmass crystallinity, with dense black material significantly having significantly higher groundmass crystallinity than grey (Figure 5). As phenocryst populations are sub-equal in both BZ and MSH clasts (Table 3), the elevated groundmass crystal contents of the black material lead to elevated bulk crystal contents in black clasts as well (Figure 5); only 1 black clast falls below 80% crystals, while no grey material rises above 80%. Also noteworthy is that one of the dense MSH clasts is holocrystalline.

3.3 Bulk and Glass H_2O Contents

Analyses of blast material from MSH presented here reproduce the findings of Hoblitt and Harmon (1993), which include a distinct decrease in bulk H_2O content with increasing clast density/decreasing vesicularity (Figure 6). Analyses of BZ material (Figure 6) indicate a similar decrease in bulk H_2O content with decreasing vesicularity, with black andesite being significantly more outgassed than grey andesite.

Using the method of Alidibirov et al. (1997), glass H_2O contents can be estimated by mass balance, whereby the bulk H_2O content of a clast is a function of the hydrous phases it contains:

$$X_{WR}^{H_2O} = \left(X_{Hbl}^{H_2O} * X_{WR}^{Hbl}\right) + \left(X_{Glass}^{H_2O} * X_{WR}^{Glass}\right) \qquad (1)$$

Hornblende (Hbl) and Glass are the hydrous phases, X^{HBL} and X^{Glass} are the weight fractions of that phase in the material of interest in the bulk rock (WR), and the X^{H2O}

Table 3: Phase proportions from BZ and MSH material. Sold phase proportions are displayed in volume % on a vesicle-free basis. Plg = Plagioclase, OPX = Orthopyroxene, Amph. = Amphibole, Ox = Fe-Ti Oxides, SiO_2 = Quartz. Bulk vesicularity is calculated from clast density after Houghton and Wilson (1989) using a dense-rock equivalent value of 2700 kg/m^3. Groundmass vesicularirty is calculated as [Bulk Vesicularity/(1 – Vol. % Phenocrysts)]. Groundmass crystallinity is defined as (Total Groundmass Crystals/ Groundmass Volume), and is displayed in volume % on a vesicle-free basis.

A. Total Phase Proportions

BZ

ρ (Kg m^{-3})	Bulk Vesicularity	Groundmass Vesicularity	Glass	Plg	OPX	Amph	Ox	SiO_2	Total ϕ
1760	35	48	26	52	9	4	2	6	74
1770	34	46	30	43	8	6	3	11	70
1840	32	46	32	43	8	5	2	10	68
1950	28	38	24	53	8	6	4	6	76
2220	18	26	17	57	7	6	2	10	83
2270	16	24	16	57	9	5	3	10	84
2370	12	19	14	49	8	5	3	21	86
2400	11	18	13	45	8	6	4	24	87
2410	11	18	19	48	9	7	3	15	81
2430	10	15	16	48	10	6	3	17	84
2440	10	16	11	51	11	5	4	19	89
2560	5	8	10	57	6	6	3	18	90
2710	0	0	14	48	10	6	3	18	86

MSH

ρ (Kg m^{-3})	Bulk Vesicularity	Groundmass Vesicularity	Glass	Plg	OPX	Amph	Ox	SiO_2	Total ϕ
1360	50	66	31	54	5	3	2	5	69
1670	38	52	31	56	4	3	2	5	69
1880	30	43	22	58	5	4	2	8	78
2250	13	20	22	58	5	4	2	10	78
2340	12	18	0	67	6	4	2	21	100
2340	10	14	13	61	5	3	2	16	87
2370	10	15	14	62	6	3	1	14	86
2430	10	14	14	61	6	3	1	15	86
2430	10	14	16	63	6	3	2	10	84

B. Groundmass

BZ

ρ (Kg m^{-3})	Bulk Vesicularity	Groundmass Vesicularity	Glass	Plg	OPX	Amph	Ox	SiO_2	Groundmass ϕ
1760	35	48	47	37	7	0	1	9	53

Table 3 (contd.)

1950	34	46	38	45	7	0	2	8	62
2220	32	46	29	47	6	0	2	16	71
2270	28	38	25	49	9	0	2	14	75
2440	18	26	16	52	7	0	2	23	84
2560	16	24	18	45	5	0	1	30	82
1770	12	19	39	41	5	0	1	13	61
1840	11	18	43	37	7	0	0	13	57
2370	11	18	17	53	6	0	1	22	83
2400	10	15	16	50	7	0	1	25	84
2410	10	16	25	51	6	0	1	17	75
2430	5	8	21	49	9	0	1	21	79
2710	0	0	18	51	9	0	1	21	82

MSH

ρ (Kg m^{-3})	Bulk Vesicularity	Groundmass Vesicularity	Glass	Plg	OPX	Amph	Ox	SiO_2	Groundmass ϕ
1360	50	66	52	37	3	0	1	6	48
1670	38	52	54	35	4	0	1	6	46
1880	30	43	37	45	4	0	1	12	63
2250	13	20	34	47	4	0	1	14	66
2340	12	18	0	66	6	0	2	27	100
2340	10	14	20	54	4	0	1	21	80
2370	10	15	22	55	3	0	1	19	78
2430	10	14	20	54	5	0	1	20	80
2430	10	14	24	57	5	0	1	13	76

C. Phenocrysts

BZ

ρ (Kg m^{-3})	Bulk Vesicularity	Groundmass Vesicularity	Groundmass	Plg	OPX	Amph	Ox	SiO_2	Total Phenocrysts
1760	35	48	72	20	3	4	1	0	28
1770	34	46	75	17	1	5	1	0	25
1840	32	46	69	25	1	4	1	1	31
1950	28	38	73	17	1	6	2	1	27
2220	18	26	68	22	2	7	1	1	32
2270	16	24	66	24	2	6	1	1	34
2370	12	19	64	26	1	6	1	2	36
2400	11	18	63	24	1	7	2	4	37
2410	11	18	60	28	2	7	1	2	40
2430	10	15	66	24	1	7	1	1	34
2440	10	16	61	26	3	6	2	2	39
2560	5	8	62	27	1	8	1	0	38
2710	0	0	63	27	1	7	1	1	37

Table 3 (Contd.)

MSH									
ρ (Kg m^{-3})	Bulk Vesicularity	Groundmass Vesicularity	Groundmass	Plg	OPX	Amph	Ox	SiO_2	Total Phenocrysts
1360	50	66	76	19	2	2	1	1	24
1670	38	52	74	22	1	2	1	1	26
1880	30	43	70	23	2	3	1	1	30
2340	13	20	66	27	2	4	1	1	34
2370	12	18	67	23	2	4	1	3	33
2430	10	14	70	22	3	3	1	2	30
2430	10	15	67	26	2	4	1	0	33
2430	10	14	69	24	2	3	1	1	31
2430	10	14	70	23	2	3	1	0	30

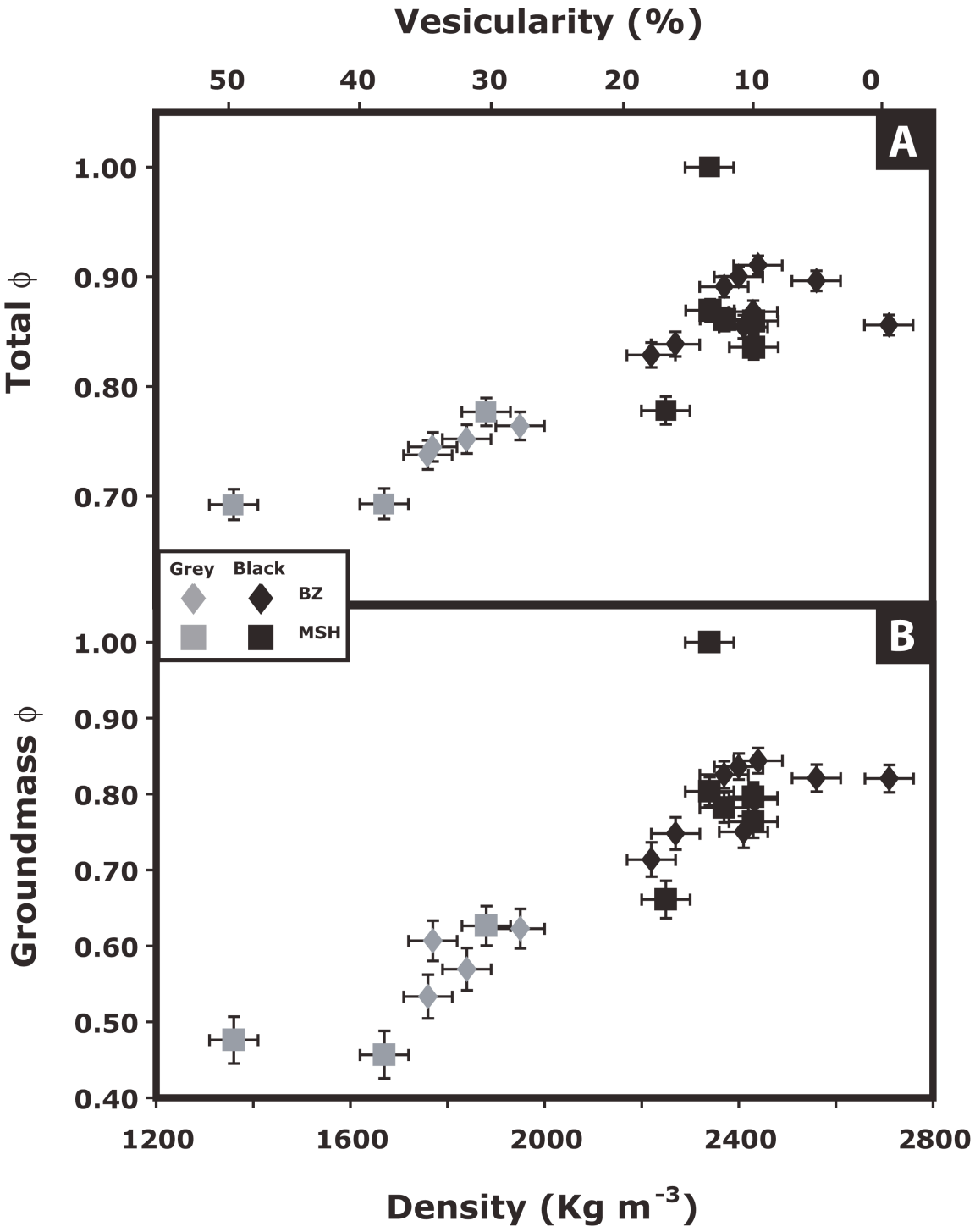

*Figure 5: Total (**A**) and groundmass (**B**) crystallinity (in volume fraction, calculated on a vesicle-free basis) of BZ and MSH blast clasts analyzed by point counting. Error bars indicate 2-σ uncertainty.*

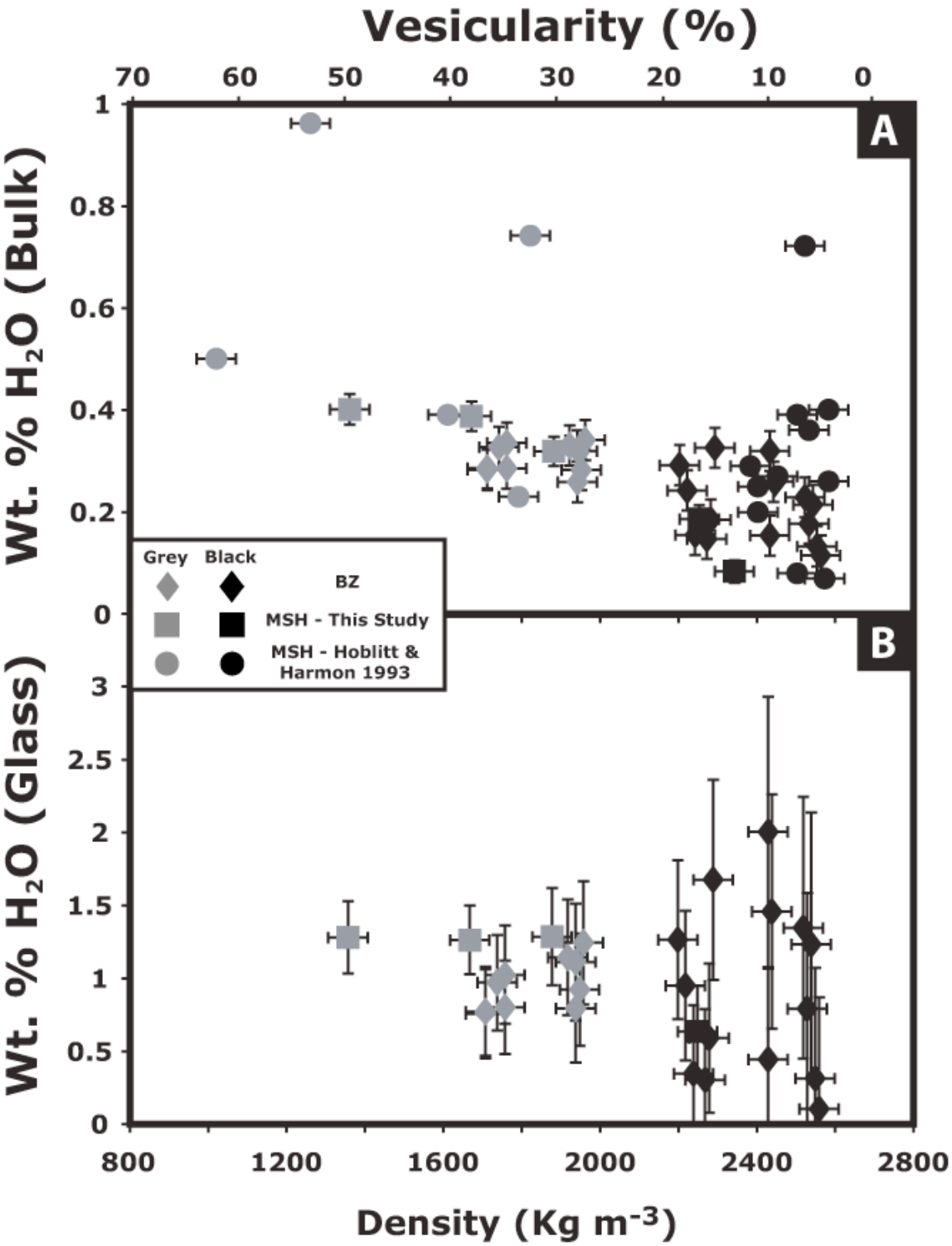

*Figure 6: **A**: Bulk H_2O contents, in weight percent, of BZ and MSH material measured by Karl Fischer Titration, supplemented with MSH data from by Hoblitt and Harmon (1993). Error bars indicate 2-σ uncertainty. **B**: Glass H_2O concentrations of BZ and MSH blast material calculated by mass balance (see text for details). Error bars indicate 2-σ uncertainty.*

terms represent the weight fraction of H_2O in the designated hydrous phase or bulk rock. Solving for the H_2O concentration in glass by algebraic manipulation:

$$X_{Glass}^{H_2O} = \frac{X_{WR}^{H_2O} - \left(X_{Hbl}^{H_2O} * X_{WR}^{Hbl}\right)}{X_{WR}^{Glass}} \qquad (2)$$

Glass H_2O contents are derived for all BZ and MSH clasts analyzed by KFT (Figure 6). The numerous uncertainties associated with each parameter on the right side of Eq. (2) lead to fairly large uncertainties in calculated glass H_2O contents. The uncertainties associated with the calculation, ±0.3-0.9 wt%, generally compare favorably to the uncertainties commonly associated with estimating glass H_2O contents by electron microprobe as the difference between analytical totals and 100% (±0.7 wt%, Devine et al. 1995; ±1 wt.%, King et al. 2002). However, they are still large relative to calculated concentration values. Nevertheless, the average calculated glass H_2O content at BZ (~1-1.5 wt%) and the value calculated by Alidibirov et al. (1997) for MSH glass (~1 wt%) fall well below the initial melt H_2O contents of 5-6 and 4.6 wt% respectively (Kadik et al. 1986, Rutherford et al. 1985). BZ blast material therefore appears similar to MSH, in that it is significantly outgassed with respect to initial magmatic values.

Glass H_2O contents can also be used to estimate pressures within the volcanic edifices prior to eruption. The average calculated glass H_2O concentrations correspond to melt H_2O solubility pressures of ~10-20 MPa (Moore et al. 1998). Of course, the measurements cannot include volatiles lost during the blast by diffusion into pre-existing vapor bubbles (e.g. Hoblitt et al. 1981), and thus these estimates are minima, though Alidibirov (1995) and Alidibirov et al (1997) suggest that such diffusion could be negligible, especially in smaller clasts. However, the 10-20 MPa range is consistent with

the pre-blast conditions assumed for MSH by the models of Kieffer (1981a) and Alidibirov (1995) and with estimates of pre-blast lithostatic pressure at MSH (Eichelberger and Hayes 1982). Notably, the release of 10-20 MPa of confining pressure is sufficient to fragment all but the densest pyroclastic material ejected by the blast stages of both volcanoes (Spieler et al. 2004).

3.4 Phase Compositions

Amphibole formulas were calculated on the basis of 23 oxygens from microprobe analyses (see Table A1), using ProbeAMPH (Tindle and Webb 1994), to classify the amphiboles under the 1997 IMA criteria (Leake et al. 1997). BZ cryptodome amphiboles are dominantly pargasite, with some edenite and mg-hornblende (Figure 7). BZ cryptodome amphiboles do not differ significantly between black and grey andesite, nor from compositions of BZ amphibole from pyroclastic flow material (Al'meev et al 1997), further supporting the cogenetic nature of BZ blast and post-blast 1956 material.

MSH clasts exhibit subtle evolution in plagioclase compositions between the grey and black material (Figure 8, Table A2). Microlite compositions in grey material evolve from An_{50} to An_{30} with progressively increasing Or content (Or_1 to Or_4). Microlites in black material include the same range of compositions as grey material, but extend to An_{25}, and greater Or content (up to Or_{10}). At BZ, the distinction between microlites in black and grey material is less clear; microlite compositions are similar between black and grey material, although four of the five most albitic grains occur in black clasts.

Glass compositions, averaged for each density fraction (Table A3, Figure A9) are projected into the Q-Ab-Or system (Tuttle and Bowen 1958) using the projection scheme

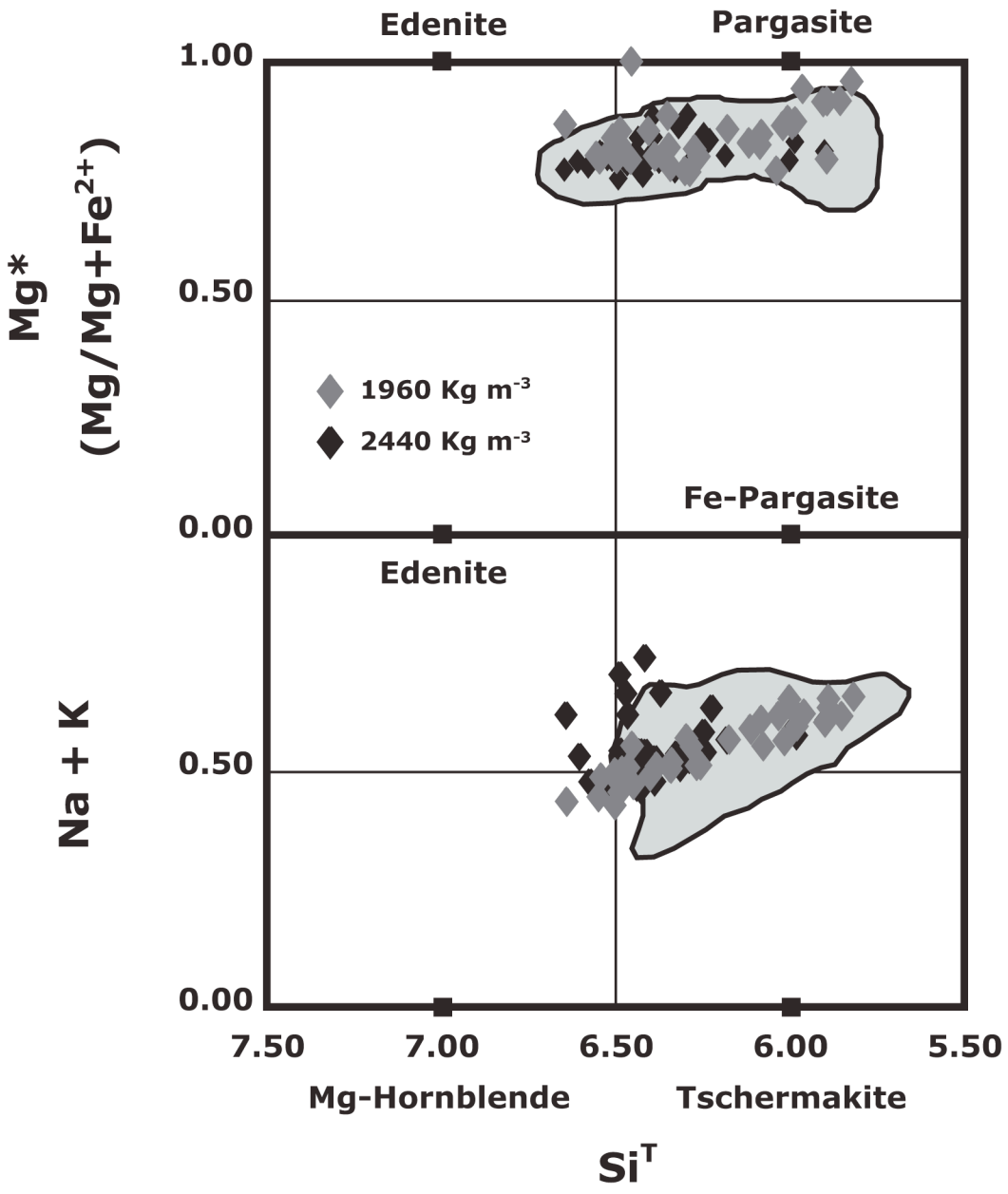

Figure 7: Compositions of BZ amphiboles for samples taken from the density modes. Grey fields represent amphibole compositions reported by Al'meev et al. (1997) for juvenile post-blast PDC samples, which were presumably stored at depth. Classification scheme is after Leake et al. (1997), with formulas recalculated using Tindle and Webb (1994). See Appendix Table A1 for a full list of compositions.

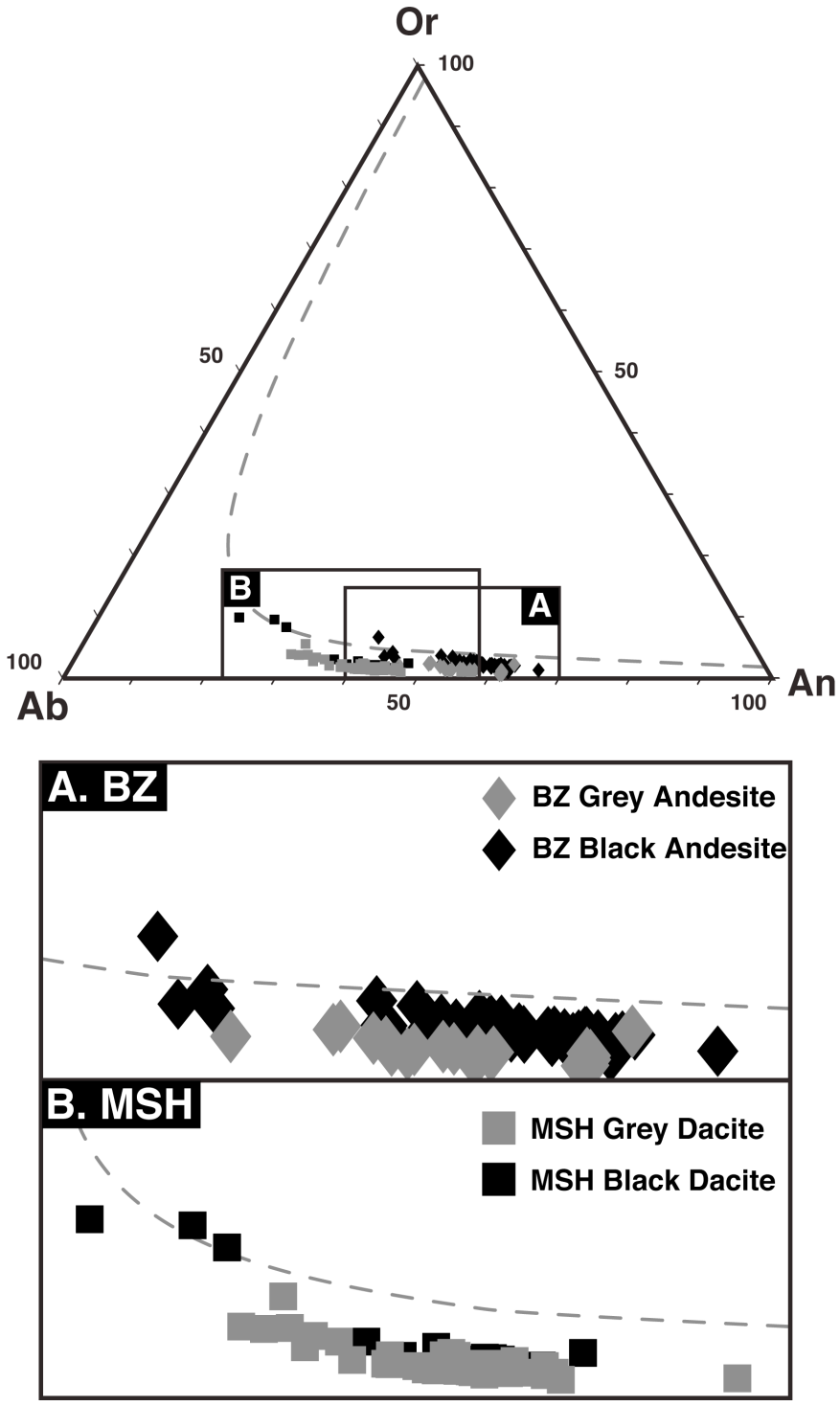

*Figure 8: Comparison of plagioclase microlite compositions from grey and black material from BZ (**A**) and MSH (**B**), projected in An-Ab-Or space, with relevant portions of the diagram expanded for clarity. Feldspar solvus (dashed grey line) calculated using SOLVCALC (Wen and Nekvasil 1994) and the thermodynamic model of Elkins and Grove (1990). See Appendix Table A4-2 for a full list of compositions.*

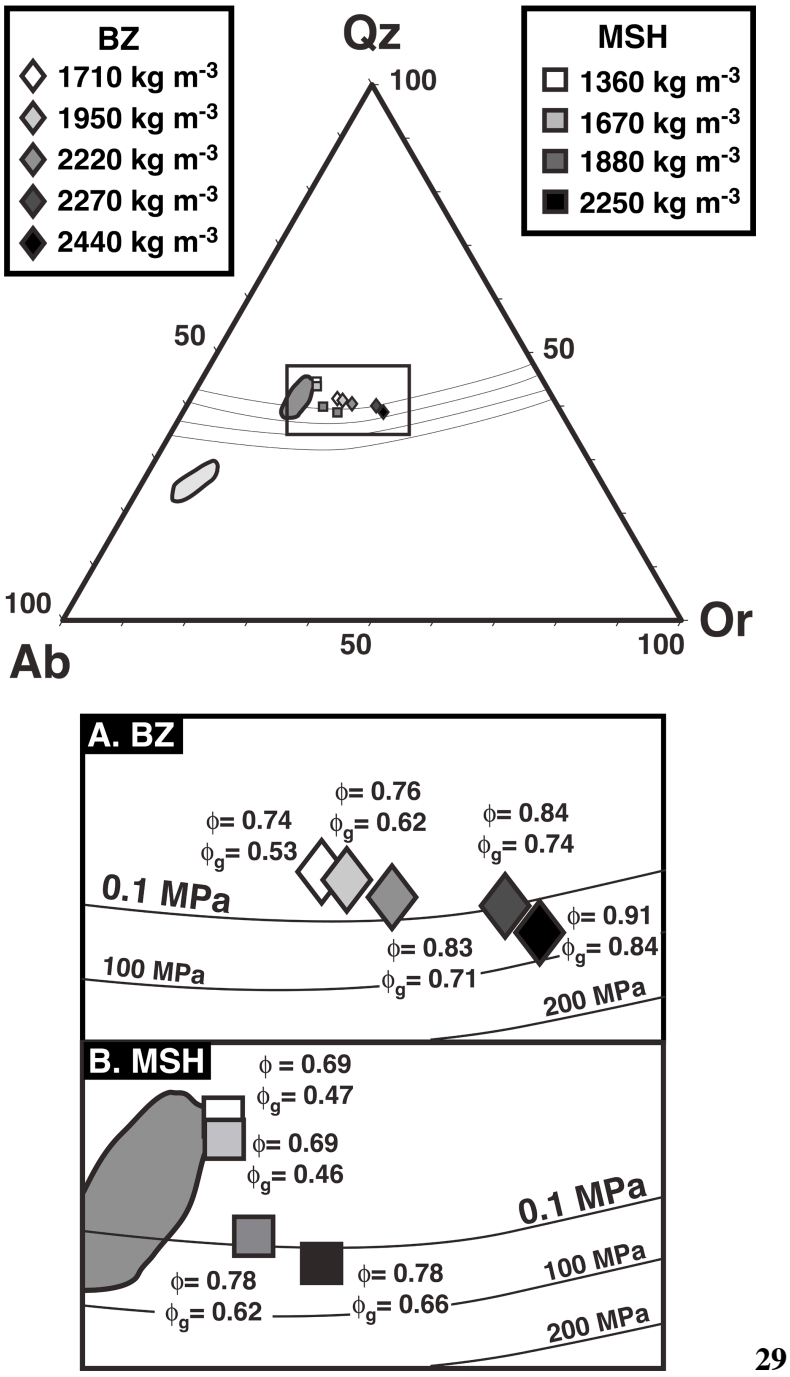

29

*Figure 9: Average compositions of groundmass glass from black and grey material, projected into the Q-Ab-Or system (see text) showing the evolution of glass compositions at BZ and MSH with increasing clast density/crystallinity. Grey and white fields indicate groundmass glass compositions of post-blast 18 May, 1980 grey and white pumice, respectively, erupted from MSH (Blundy and Cashman (2001). Inset box on ternary diagram is separated into BZ (**A**) and MSH (**B**) for clarity. The crystallinity of each clast is also noted (ϕ = bulk volume fraction of crystals, ϕ_g = volume fraction of crystals in groundmass). See See Appendix Table A3 for a full list of compositions.*

of Blundy and Cashman (2001), with refinement of the 0.1 MPa cotectic by Brugger et al. (2003). BZ glasses (Figure 9A) progress from more primitive to more evolved (Blundy and Cashman 2001) compositions with increasing crystallinity along the 0.1 MPa cotectic, indicating melt evolution driven by low-pressure crystallization. MSH glasses (Figure 9B) also progressively evolve with increasing crystallinity, though unlike at BZ, compositions overshoot the 0.1 MPa cotectic, the result of apparent silica oversaturation.

3.5 Hydrogen Isotopes

Hydrogen isotopic compositions of eruptive products are modified from magma reservoir values by open- and closed-system fractionation due to degassing prior to the blast (Taylor et al. 1983, Taylor 1986, Newman et al. 1988, Dobson et al. 1989, Hoblitt and Harmon 1993, Harford et al. 2003). Closed-system fractionation, whereby melt and exsolved vapor remain in continuous isotopic equilibrium, can be modeled by:

$$\partial D_f = \partial D_i + (1 - F)10^3 \ln \alpha_{v-m} \quad \text{(A1)}$$

Open-system fractionation is modeled by Rayleigh fractionation:

$$\partial D_f = \partial D_i + 10^3 (F^{\alpha_{v-m}-1} - 1) \quad \text{(A2)}$$

Where ∂D_f and ∂D_i are the final and initial ∂D values (‰ SMOW), F is the weight fraction of H_2O in melt, and $\alpha_{V\text{-}M}$ is the melt- H_2O fractionation factor. This fractionation factor is dependant on melt H_2O-OH speciation, and is calculated using Equation 9 of Taylor (1986):

$$\alpha_{v-m} = X_{H_2O_m} \alpha_{v-H_2O_m} + (1 - X)_{OH_m} \alpha_{v-OH_m} \quad \text{(A3)}$$

Where X_{H2Om} and $(1\text{-}X)_{OHm}$ are the relative H_2O and OH abundances and $\alpha_{V\text{-}H2Om}$ and $\alpha_{V\text{-}OHm}$ are the vapor- H_2O and vapor-OH fractionation factors. Values of 1.040 and 0.985 are

assumed for $\alpha_{V\text{-}OHm}$ and $\alpha_{V\text{-}H2Om}$ respectively; appropriate values for degassing from a rhyolitic melt (Dobson et al. 1989). VolatileCalc (Newman and Lowenstern 2002) is used to determine H_2O-OH speciation.

Closed-system behavior is assumed to dominate until the magma becomes sufficiently permeable to allow for open-system degassing. The vesicularity required for this permeability is still a subject of some debate, but could be anywhere from 30% (Blower 2001) to 60% (Eichelberger et al. 1986) vesicularity; The lower limit of 30% identified by Blower (2001) will be used in this study, though admittedly the critical porosity could be significantly higher (e.g. Eichelberger et al. 1986, Takeushi et al. 2005). The method of Martel et al. (1998) is used to calculate the change in vesicularity with depth at BZ. 30% vesicularity is reached at ~2000 m (~41 MPa, assuming a lithostatic load with a density of 2100 kg m^{-3}). According to the solubility model of Moore et al. (1998), BZ melt would contain ~2.5 wt% H_2O at 2000 m. This depth and pressure is assumed to be the extreme limit of the depth at which open-system degassing could begin. Hoblitt and Harmon (1993) assume that the minimum depth for the onset of open-system behavior at MSH is the top of the cryptodome. At BZ, the 800 m wide crater at the summit exposed a small portion of the cryptodome to the atmosphere, (Gorshkov 1963, Belousov 1996) so under the Hoblitt and Harmon (1993) assumption, the minimum pressure for the onset of open-system degassing is approximately atmospheric, equivalent to ≈0.1 wt.% H_2O (Moore et al. 1998). However, at low melt H_2O contents, water exists almost exclusively as hydroxyl (OH) groups (Silver et al. 1990), and kinetic effects begin to dominate ∂D fractionation (Anderson and Fink 1989). Therefore, a value of 0.4 wt. %

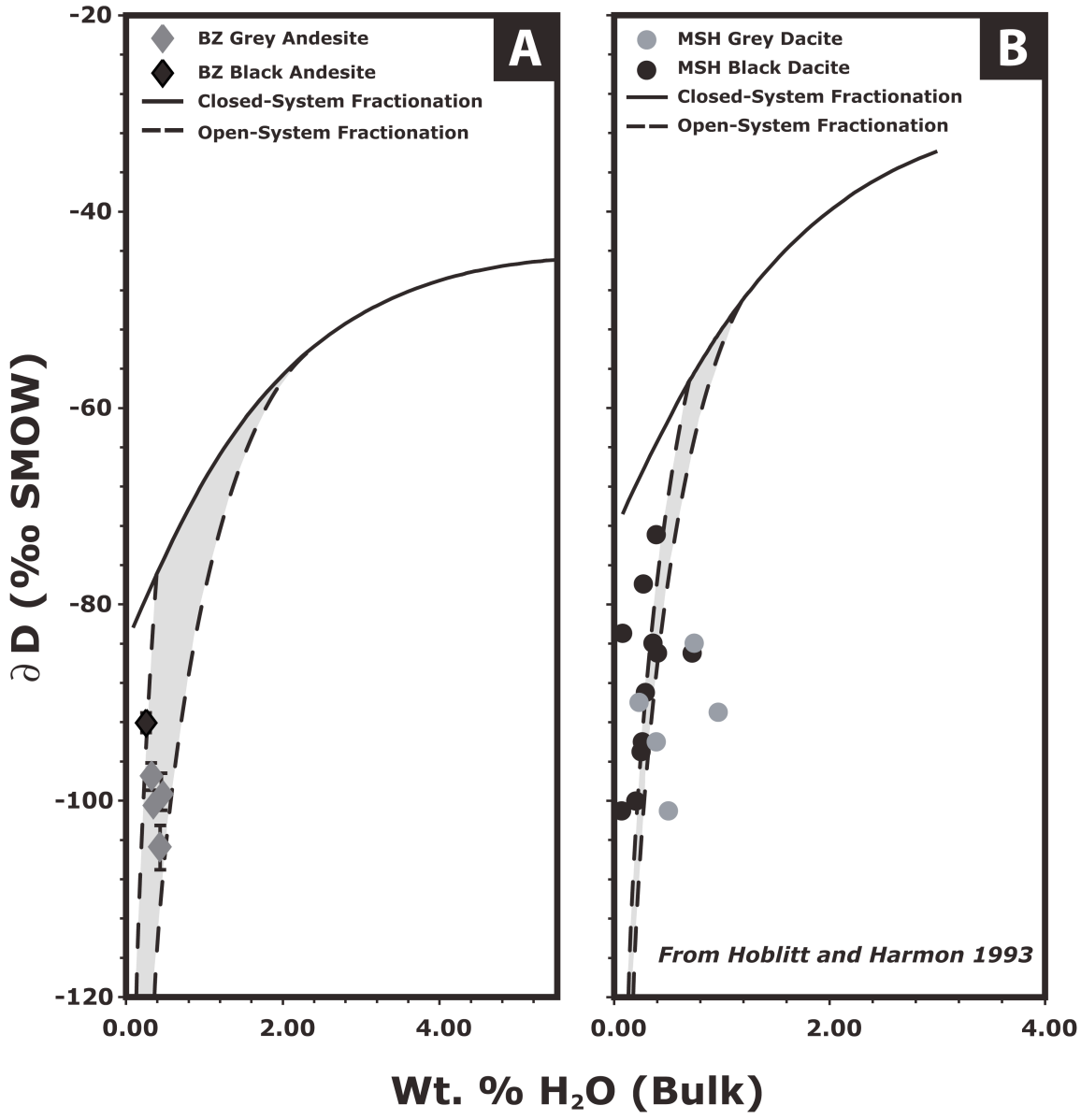

Figure 10. ***A****. ∂D values of BZ bulk rock material shown in relation to modeled ideal open- and closed-system ∂D fractionation paths (see text for details). Values plotted are the average of 4 repeat analyses, with error bars representing the reproducibility of the isotopic value obtained. Shaded areas represent the envelope enclosed by perfect closed-system fractionation paths beginning at minimum and maximum H_2O contents (see text for details). Isotopic data and fractionation paths for MSH material, determined by Hoblitt and Harmon (1993), are shown in* ***B*** *for comparison.*

H_2O, equivalent to ≈100 m below the top of the BZ cryptodome, is assumed. Fractionation paths are modeled for BZ assuming an initial ∂D value for BZ melt of –45‰ (Pineau et al. 1999), and an initial melt H_2O content of 5.5 wt. % (Kadik et al. 1986), and compared to the fractionation curves of Hoblitt and Harmon (1993). Although the sample set for BZ is somewhat limited, ∂D data for both blast and post-blast material is best explained by shallow open-system fractionation (Figure 10), as is the case for MSH, related to the outgassing of the cryptodome material during ascent, emplacement and storage within the edifice.

4. DISCUSSION

4.1 Origin of Holocrystalline MSH Material

Holocrystalline material has not been identified previously in the MSH blast deposits; therefore, before the implications of the crystal and volatile contents of MSH clasts can be commented on, their juvenile nature must be verified. The holocrystalline black MSH clast (Figure 5) shows no signs of alteration, and is indistinguishable in hand specimen from other black dacite. This clast contains the same phase assemblage of plagioclase, orthopyroxene, quartz, amphibole with well-developed reaction rims, Fe-Ti oxides, trace apatite and K-feldspar, as is found in other 1980 MSH eruption products (Rutherford et al. 1985, Rutherford and Hill 1993). The compositions of plagioclase crystals span the same range (though also extending it) as in glass-bearing MSH blast clasts. This clast was analyzed for major element chemistry by XRF, and has almost the exact same major element composition as the grey and glass-bearing black MSH material (Table 4) and the compositions reported in Hoblitt and Harmon (1993). Therefore, this

Table 4: Comparative XRF analyses of holocrystalline and glass-bearing MSH blast dacite. Oxides are in wt. % with all Fe as Fe_2O_3.

ϕ (Vol.%)	69	69	69	78	100
SiO_2	64.7	65.0	64.9	64.7	64.4
TiO_2	0.64	0.62	0.63	0.59	0.64
Al_2O_3	17.3	17.6	17.4	17.6	17.2
Fe_2O_3*	4.49	4.52	4.52	4.56	4.52
MnO	0.07	0.08	0.08	0.08	0.07
MgO	1.78	1.79	1.87	1.86	1.86
CaO	4.87	4.89	4.80	4.92	4.89
Na_2O	4.60	4.49	4.59	4.41	4.59
K_2O	1.36	1.35	1.36	1.33	1.33
P_2O_5	0.09	0.09	0.10	0.10	0.08
Total	99.9	100.4	100.2	100.1	99.6
LOI	1.09	0.80	0.67	0.14	-0.01

holocrystalline clast is probably juvenile MSH material that attained 100% crystallinity. At 880°C (the inferred magmatic temperature for MSH, Rutherford et al. 1985), and under very low pressure (10-20 MPa) conditions, MSH magma is at near-solidus, or possibly sub-solidus conditions (see Figure 3 of Rutherford and Hill 1993). The holocrystalline clast probably represents a portion of the MSH blast material that approached equilibrium at sub-solidus conditions, and may represent some of the first-intruded magma, which had the longest time to crystallize within the cryptodome. Fully crystalline non-juvenile material is also present in the MSH blast deposits.

4.2 Heterogeneous Pre-Blast Outgassing

The most probable explanation for the generally lowered H_2O contents observed in black clasts is that the magma that did not experience bubble growth during the blast had been stored within the volcanic edifice longer prior to fragmentation, and had more time to outgas than the magma destined to become grey clasts. The deformation patterns in the of the edifices at both BZ and MSH during the periods of cryptodome growth preceding the blasts indicates that magma input into the cryptodome was probably quasi-continuous, rather than instantaneous (Gorshkov 1959, Lipman et al. 1981a), and likely was at a maximum in the initial phases of cryptodome emplacement (Voight et al. 1981, Belousov et al. 2007). Therefore the magma that first reached the cryptodome would have had longer to lose volatiles by outgassing (Hoblitt and Harmon 1993).

4.3 Evolution Of Crystallinity and Phase Compositions

The progression of groundmass glass compositions towards more evolved compositions with increasing density and groundmass crystallinity (Figure 9) probably results from progressive crystallization, which leads to the disparity in overall crystal content between black and grey material. Primitive MSH matrix melt compositions from the most vesicular, least crystalline grey material studied here are similar to the grey blast pumice analyzed by Blundy and Cashman (2001) and are more silica-rich than would be expected even at 0.1 MPa (Figure 9). Crystallization of quartz in the groundmass then returns the MSH samples to cotectic proportions in more microlite-rich material, with the initial silica excess a result of the kinetically-induced "lag" in quartz nucleation and crystallization observed by Brugger et al. (2003). At BZ, no such overshoot is observed; quartz is nearly ubiquitous in the post-blast Plinian-phase samples (Gorshkov and Bogoyavlenskaya 1965, Plechov et al. 2008), indicating that the onset of quartz crystallization probably occurred earlier than at MSH. Instead, BZ matrix melt evolves essentially along the 0.1 MPa cotectic with increasing crystallinity.

While cooling-induced crystallization has been observed in other shallow magma bodies such as dikes (e.g. Cashman 1993) and lava lakes (e.g. Wright and Okamura 1977), it seems unlikely to be the cause of the compositional evolution of BZ and MSH glasses. Direct and remote measurements of temperatures within post-1980 MSH extrusive domes were consistent with measurements of magmatic temperatures by mineral geothermometers (Rutherford et al. 1985), indicating that the temperature in the interior of such domes does not deviate from crustal magmatic storage conditions over time scales comparable to the periods leading up to the BZ and MSH blasts (Dzurisin et

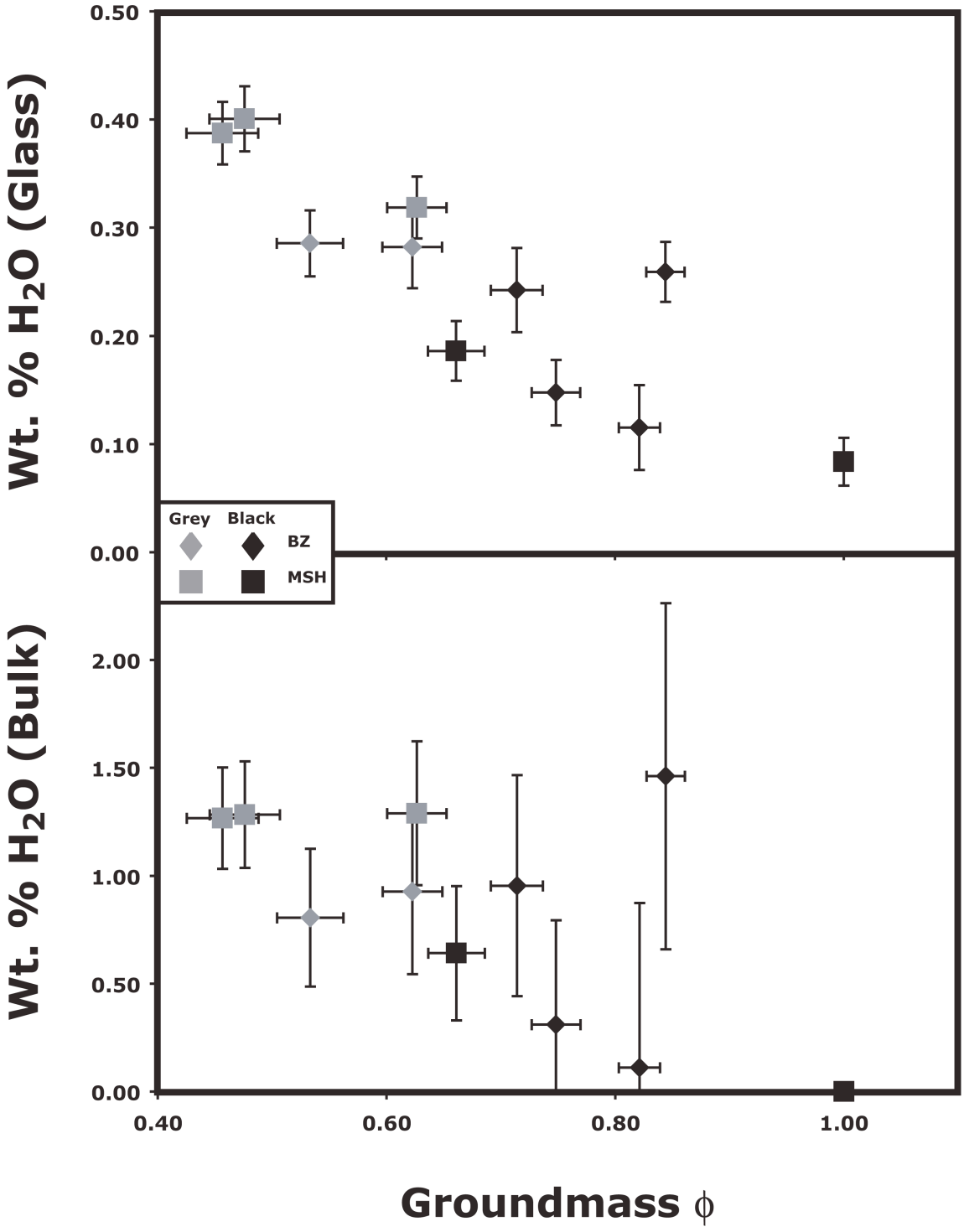

Figure 11: Groundmass crystal fraction (on a vesicle-free basis) of BZ and MSH blast material related to bulk and glass H_2O content. More degassed samples show higher crystal contents than more volatile-rich samples, though some more crystalline material appears to retain higher H_2O content.

al. 1990, Schneider et al. 2008). Furthermore, based on both conductive cooling models and cooling rates determined by studies of progressive magnetization (Dzurisin et al. 1990), Hoblitt and Harmon (1993) estimate that the chilled margins of the BZ and MSH cryptodomes would be no wider than a few meters, probably accounting for ≤5% of the total volume of each cryptodomes. The same geometry is assumed here for the BZ cryptodome. The high bulk crystallinity black material accounts for ~65% of the total blast volume at BZ (Belousov et al. 2007) and 28% of the deposits at MSH (Hoblitt and Harmon 1993), so it would seem improbable that cooling-driven crystallization could generate the crystallinity disparity between black and grey material (Figures 5, 11). Hoblitt and Harmon (1993) assumed that the MSH cryptodome was a near-spherical body cooling from the outside, a reasonable approximation given (a.) the geometry, endogenous growth and cooling behavior observed in non-fragmented silicic cryptodomes (e.g. Goto and McPhie 1998, Stewart and McPhie 2003) and (b.) that magma empacement was at a maximum in the earliest stages of cryptodome emplacement (Voight et al. 1981), meaning that the geometry of the cryptodome was likely established early in the cryptodome-building stage.

Cashman (1988, 1992) inferred magmatic degassing as the likely driving force for groundmass crystallization within the MSH dome. The same process is likely in play at BZ, and therefore the difference in groundmass crystallinity between black and grey material probably reflects the differential degassing of BZ and MSH cryptodome melts, as more outgassed clasts are generally more crystalline than more volatile-rich material (Figure 11). Cryptodome magma from both MSH and BZ had pre-blast melt H_2O contents below the concentrations required by the equilibrium phase assemblage, and the

resultant increase in liquidus temperatures probably resulted in an effective undercooling to drive microlite growth (e.g. Geschwind and Rutherford 1995). At both BZ and MSH, not only is outgassing sufficient to drive groundmass crystallization within the entire cryptodome (e.g. Cashman 1992), but the combination of longer edifice residence and greater degree of outgassing (and therefore higher liquidus temperatures) inferred for magma that became black pyroclasts may have allowed higher degrees of groundmass crystallization, and cause the interstitial melt to progress to more evolved compositions.

4.4 Models For The Formation Of Bimodal Density Distributions

The origin of the bimodal density distributions associated with laterally directed explosions has been addressed previously in varying degrees of detail (Hoblitt and Harmon 1993, Alidibirov et al. 1997, Cashman and Hoblitt 2004, Belousov et al. 2007), with the dominant mechanism inferred to be the heterogeneous distribution of volatiles within the cryptodome prior to fragmentation. This interpretation is supported by the data presented herein; the volatile contents and LOI's of grey and black material differ at both BZ and MSH (Figure 6, Table 2). If the magma that remained dense lacked both volatiles and vesicles prior to the blast (e.g. Hoblitt and Harmon 1993, Alidibirov et al. 1997), it would seem impossible for that magma to vesiculate during fragmentation. However, the new measurements of crystallinity (Figure 5) and bulk H_2O (Figure 6) suggest another rheologic factor could be in operation.

While much of the black material is volatile poor compared to the grey, several clasts at BZ exceed the average bulk H_2O content of grey material (0.30 wt%); Hoblitt and Harmon (1993) even report one black MSH clast with greater than 0.75 wt% bulk

H_2O. The similarity in volatile content of grey and some black blast material may partly be an artifact of syn-blast H_2O diffusion; however it still seems likely that, while generally outgassed, a portion of the magma from which the black material was derived was at least comparable in volatile content to the cryptodome magma that became grey clasts. As stated previously, the determination of glass H_2O content by mass balance (Figure 6) is subject to high degrees of uncertainty. The data do indicate, however, that some of the glass H_2O concentrations in black BZ material may be as high as 2-3 wt%, greater than the equilibrium solubility value (~1.4 wt%) for H_2O in BZ melt at the base of the cryptodome (approximately 750 m depth, Belousov et al. 2007), and higher than the average grey BZ glass H_2O values (~1 wt. %). Black material also may not be completely devoid of vesicles. Both volatile-poor and volatile-rich black material contain abundant pores (Figure 12), and though some of these may be diktytaxitic voids (the result of the decrease in volume that a magma undergoes as it crystallizes), the abundance of small pores could indicate that rather than being lost to outgassing, bubbles may have been present in the magma that became the black material, but were restricted from expanding during the blast (e.g. Proussevitch and Sahagian 1998). If volatile content is the dominant controlling factor in determining whether or not a clast can vesiculate during a volcanic blast, why then did some volatile-charged black material remain dense?

Quenching due to cooling along the margins of the cryptodome potentially locks in elevated volatile contents. Of the BZ and MSH black material, ~65 and 70% of the black clasts analyzed have greater than 0.2 wt% H_2O, the lower limit of the vesiculation threshold proposed by Hoblitt and Harmon (1993), and ~20 and 30%, respectively, of clasts analyzed have bulk H_2O greater than 0.3 wt% (the median threshold value). Black

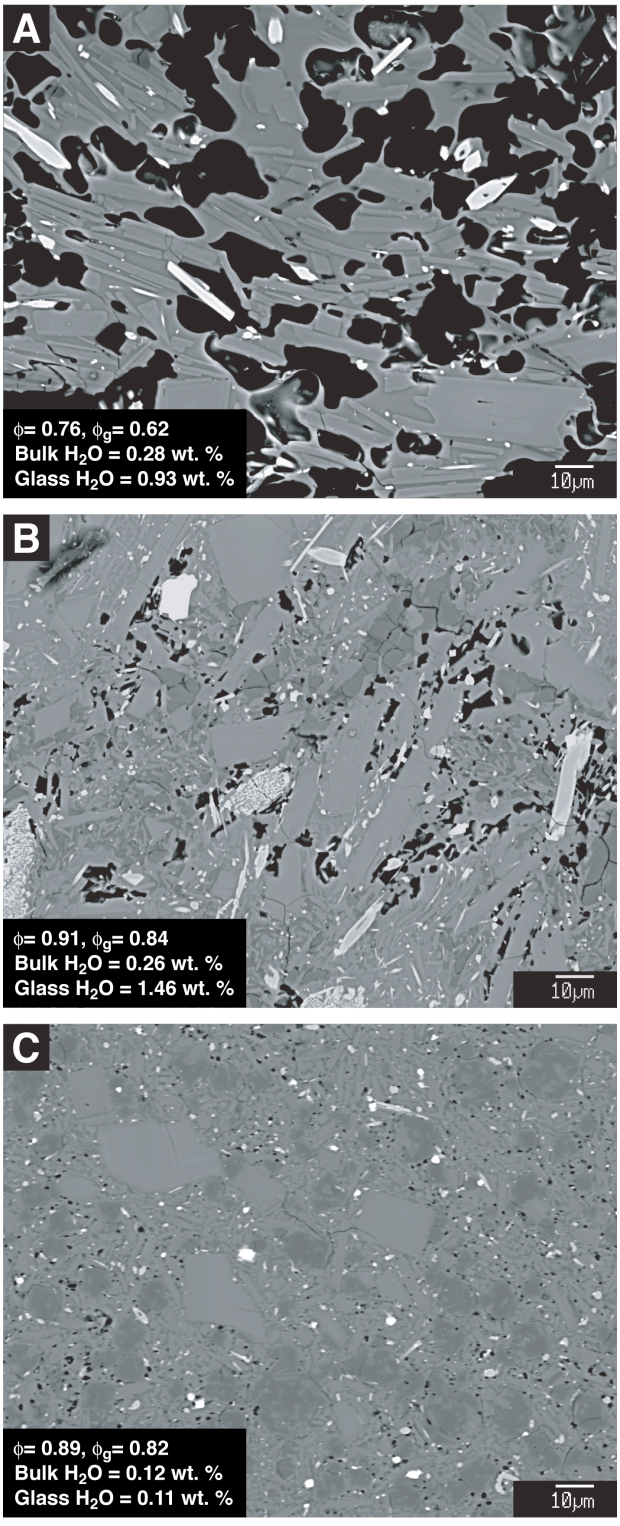

*Figure 12: Comparison of pore textures in (**A**) grey blast material, (**B**) volatile-rich black material and (**C**) volatile-poor blast material from BZ. Bulk and groundmass crystal volume fraction (ϕ and ϕ_g), bulk H_2O and calculated groundmass glass H_2O are displayed for each sample.*

material accounts for 65 and 28% of the total volume of blast material from the BZ and MSH eruptions (Hoblitt and Harmon 1993, Belousov et al. 2007); therefore if this sample set is assumed to be representative, ~10-40 and 9-20% of the BZ and MSH cryptodomes, respectively, would have consisted of magma that remained dense, despite having volatile contents potentially sufficient to vesiculate during decompression. The calculations of Hoblitt and Harmon (1993) showed that the quenched margins may account for no more than 5% of the cryptodome (and possibly quite a bit less). Thus, while post-emplacement quenching along cryptodome margins could account for some of the volatile-rich black material, it cannot account for all of it.

The rheology of highly-crystalline silicic magmas is a highly complex subject, due to the large numbers of parameters that have been identified as important in volcanic environments. At high solid fractions ($\phi > 0.5$), magmas are non-Newtonian fluids, with rheological behavior dependent on strain rate (e.g. Stevenson et al. 1996, Vigneresse and Tikoff 1999, Lavallée et al. 2009) and on the rate of applied stress (e.g. Dingwell 1997). Though the viscosity of the interstitial melt loses influence at higher solid fractions (Lavallée et al. 2009), it does play some role and can vary over several orders of magnitude depending on melt H_2O content and temperature (e.g. Giordano et al. 2008). Crystal size and shape, and heterogeneities therein, control the effects of crystal-crystal interactions on rheology, such as the onset of non-Newtonian behavior and development of yield strength (e.g. Yu and Standish 1993, Hoover et al. 2001, Ishibashi and Sato 2007). Although models for the rheological behavior and emplacement of highly crystalline magmas continue to improve (e.g. Costa et al. 2009, Massol and Jaupart 2009), no widely-accepted standard model exists for how highly crystalline magmas

respond to applied stress. Undoubtedly, however, assuming all other parameters (applied stress, temperature, melt viscosity, etc.) are equal, a more crystalline magma will be more viscous than a magma with a smaller solid fraction (Petford 2003).

The bulk crystallinity of BZ and MSH blast material essentially changes as a function of groundmass crystallinity, as the phenocryst proportions are subequal across the range of densities. Furthermore, the bulk crystallinity shows a continuum very similar to the density trend seen in BZ and MSH blast material, and is indeed well correlated with density; if 2000 kg/m^3 is accepted as the threshold between black and grey material (Hoblitt and Harmon 1993), then all grey material falls in the range of $\phi = 0.70 - 0.78$, while all black material except 1 MSH clast falls above $\phi = 0.80$ (Figure 5). While this range of crystallinity seems small, at high crystal fractions, the difference in viscosity between a magma body with $\phi = 0.70$ and $\phi = 0.80$ could be as a few orders of magnitude (Figures 2 and 3 of Costa et al. 2009, and references therein), and increased magma viscosities have been shown to retard or even halt bubble growth completely (Thomas et al. 1994, Toramaru 1995, Barclay et al. 1995, Proussevitch and Sahagian 1998). This suggests that rheological factors might have prevented the volatile-charged, highly crystalline magma from vesiculating during cryptodome fragmentation (Figure 13). Interestingly, the crystallinity threshold between grey and black material is similar to the Particle Locking Threshold (PLT) of Vigneresse et al. (1996). The PLT occurs at $\phi > 0.70$-0.75 (or possibly higher, depending on the sizes and shapes of the crystals involved), above which the melt phase loses connectivity, and the rheology of the magma passes from Bingham fluid behavior to plastic, high yield-strength solid behavior

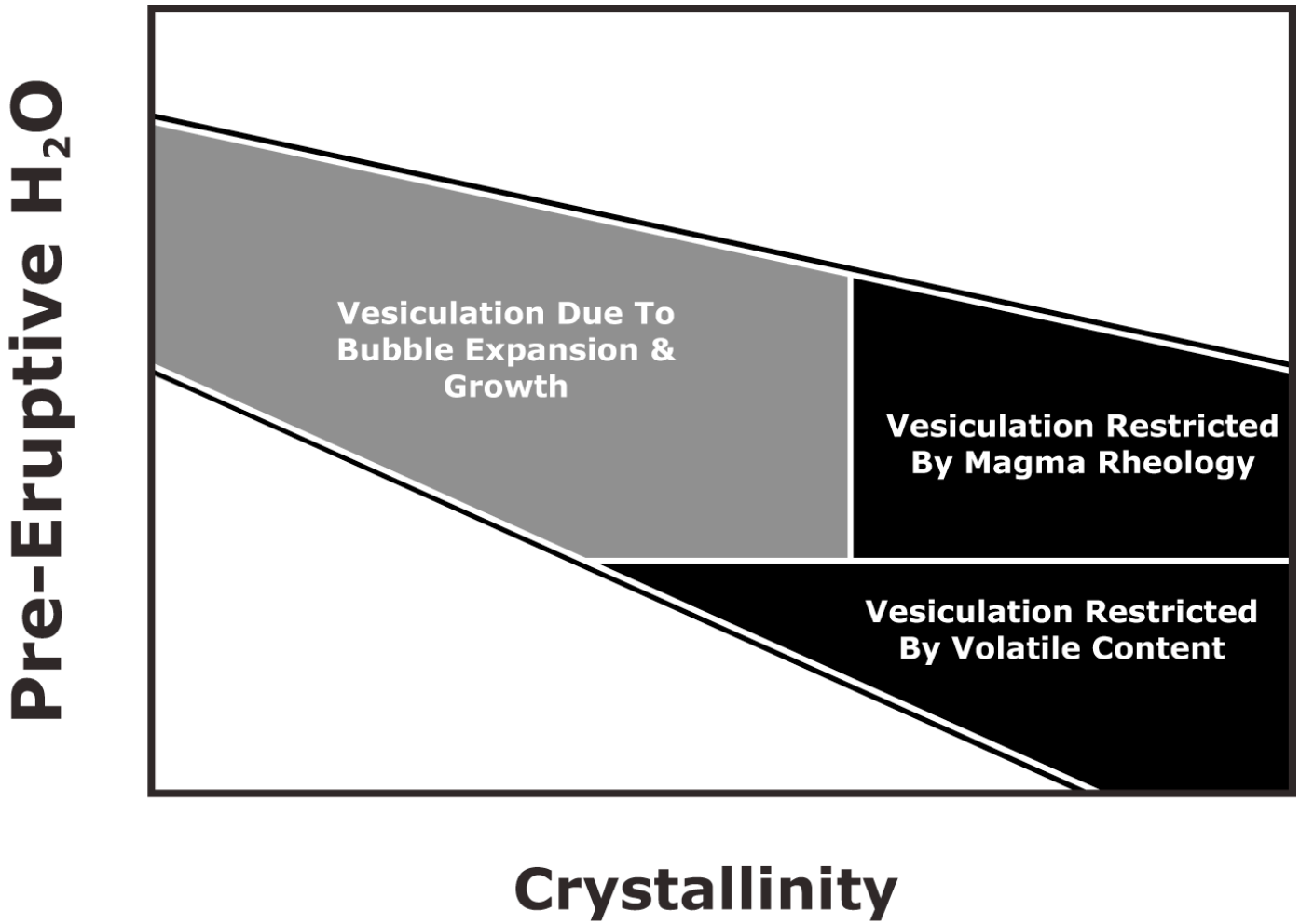

Figure 13: Schematic representation of how crystallinity and volatile content thresholds inhibit syn-blast bubble expansion of dome material.

(Vigneresse et al. 1996, Hrouda et al. 1999). The PLT is formulated for magmas crystallizing and deforming in a plutonic setting, and may not be strictly relevant to volcanic blasts, in which the applied rates of strain are much higher. However, the loss of melt connectivity at $\phi \sim 0.75$ may represent a point where crystal-crystal interactions prevent vesicles from expanding during a volcanic blast, giving rise to black material.

4.5 Implications for Pyroclastic Deposits

Thresholds in crystallinity and volatile content may explain why the relative abundances of the black and grey material at BZ contrast with those at MSH. At BZ, the black mode is dominant (~65% Belousov et al. 2007), while at MSH the grey mode is dominant (~72%, Hoblitt and Harmon 1993), and less dense than the BZ grey material (Figure 2). If magma flux was at a maximum in the early stages of cryptodome formation (Voight et al. 1981, Belousov et al. 2007), then a significant portion of cryptodome magma would have been emplaced early in each eruption. However, at BZ, this magma would have had more than four months to outgas and crystallize – a process made easier by the exposure of a small portion of the dome at the summit (Belousov 1996) – while MSH magma would have had only two. If the BZ magma was in the cryptodome longer, and could outgas more easily, it would have had more time to outgas and crystallize beyond the volatile and crystallinity thresholds proposed previously (Hoblitt and Harmon 1993) and in this study, resulting in the dominance of the black mode seen in the BZ deposits, and the denser nature of the BZ grey ejecta.

4.6 Implications for Eruptive Style

The negative correlation between crystal content and syn-blast vesiculation could have significant effects on eruptive style in a variety of volcanic settings. Spieler at al. (2004) showed that the amount of energy necessary to fragment a melt increases with decreasing melt porosity. If high crystal contents exert some control over vesiculation and bubble expansion, then the efficiency of magma fragmentation will be in part controlled by the crystallinity of that magma. Belousov et al. (2002) report the occurrence of similar control during the 1997 eruption of BZ, where the high crystallinity and limited vesiculation of juvenile material ejected in the opening phases of the eruption favored the production of block and ash flows, while the introduction of less crystalline, more volatile-charged magma stored at depth allowed for more intense fragmentation and the development of a partially stable eruptive column. Gardner et al. (1998) proposed that increasing microlite contents, driven by degassing, led to higher energies necessary to drive fragmentation during the 1992 eruption of Crater Peak, Alaska, and the eventual termination of the eruption when the magma became too degassed and crystalline to ascend.

These observations could be applicable to the BZ and MSH blasts: does the degree of outgassing and crystallization prior to the fragmentation of a silicic cryptodome influence the power of the directed blast it produces? Although the BZ blast is volumetrically larger, and was produced by a larger cryptodome than the correlative blast deposit at MSH, it covered an area 100 km^2 smaller (Hoblitt et al. 1981, Hoblitt and Harmon 1993, Belousov 1996), and was far more laterally confined (Figure 3). Furthermore, the MSH blast encountered topographic features that impeded transport,

though they may also have promoted lateral expansion (Hoblitt et al. 1981), whereas the BZ blast traveled down smooth, more steeply dipping terrain (Belousov et al. 2007). Was the BZ blast less powerful? If a greater proportion of material at BZ was prevented from vesiculating syn-blast due to low volatile content (e.g. Hoblitt and Harmon 1993) and high bulk crystallinity, the blast would have been less powerful because the cryptodome magma (a) possessed less potential energy for expansion and (b) was less efficient in expelling the stored energy it did possess. More models of blast dynamics at BZ and comparison to established estimates of energy released at MSH (e.g. Kieffer 1981b) are needed to address these inferences.

5. CONCLUSIONS

1. The heterogeneity in the open-system outgassing of BZ blast material mirrors that seen at MSH (Hoblitt and Harmon 1993), with dense, black ejecta being generally more outgassed than vesicular, grey ejecta. At both BZ and MSH, interstitial melt in blast material is significantly degassed relative to crustal storage conditions.
2. While black material is in general more outgassed than grey at both MSH and BZ, there is a portion of black material that contained at least comparable volatiles to grey material. Therefore the dense nature of the black material can only be partially ascribed to inhomgeneous outgassing.
3. Melt degassing in the volcanic edifices of both BZ and MSH probably drove significant crystallization after the formation of the cryptodome. This crystallization is reflected in the heightened groundmass crystallinity (and, consequently, bulk

crystallinity) of black material relative to the grey, and in glass compositions, which become progressively more evolved in black material.

4. This crystallinity discrepancy suggests a link between heightened crystallinity and syn-blast vesiculation process, such that some of the black material derived from a portion of the cryptodome magma that was unable to vesiculate during the blast due to rheological considerations (Figure 13), despite being relatively rich in volatiles. The remaining black material derived from cryptodome magma that did not vesiculate during the blast due to extensive outgassing prior to fragmentation (e.g. Hoblitt and Harmon 1993).
5. The longer cryptodome-building period at BZ, and the more open nature of the BZ cryptodome, led to the attainment of critical values of volatile deficiency and crystal content, beyond which syn-blast vesiculation cannot occur, in a large proportion of the BZ cryptodome magma than in the MSH cryptodome. This probably led to the dominance of the black mode at BZ, contrasting with MSH where the cryptodome emplacement period was shorter and the grey mode was dominant. Improved models of the fluid dynamics of the BZ blast will help answer whether a real difference in the power of the BZ and MSH blasts exists, and what roles pre-blast outgassing and crystallinity play in such a discrepancy.

APPENDIX TABLES

Table A1: Microprobe analyses of BZ hornblende. Density in kg/m^3.

Density	2440	2440	2440	2440	2440	2440	2440	2440	2440	2440	2440
Grain	1	1	1	2	2	2	3	3	3	4	4
Core/Rim	Core	Core	Core	Core	Core	Core	Core	Core	Core	Core	Core
SiO_2	46.2	45.9	46.6	41.9	41.0	44.6	45.8	45.4	45.5	43.8	45.5
TiO_2	1.87	1.94	1.92	2.16	2.29	1.83	1.76	1.77	1.90	1.95	2.08
Al_2O_3	9.6	10.0	9.4	14.0	14.4	11.1	10.1	10.2	10.2	11.8	10.1
FeO	14.1	14.2	13.9	14.9	14.8	14.7	13.6	13.8	14.1	14.7	14.0
MnO	0.32	0.33	0.32	0.30	0.32	0.29	0.34	0.37	0.36	0.38	0.33
MgO	13.5	13.5	13.8	12.1	12.0	13.5	13.6	13.5	13.5	12.6	13.4
CaO	11.3	11.2	11.1	11.2	11.1	10.8	11.1	11.0	10.9	11.1	11.1
Na_2O	1.49	1.44	1.68	1.84	1.94	1.60	1.47	1.46	1.75	1.69	1.56
K_2O	0.44	0.42	0.46	0.45	0.44	0.45	0.36	0.38	0.40	0.42	0.34
Cl	0.05	0.05	0.04	0.04	0.03	0.06	0.06	0.06	0.05	0.05	0.06
Total	98.9	99.0	99.2	98.9	98.4	99.0	98.1	97.9	98.5	98.4	98.4
Si	6.58	6.53	6.61	6.01	5.91	6.32	6.55	6.52	6.50	6.29	6.51
Al^{iv}	1.42	1.47	1.39	1.99	2.09	1.68	1.45	1.48	1.50	1.71	1.49
Al^{vi}	0.20	0.20	0.18	0.37	0.35	0.18	0.25	0.24	0.20	0.28	0.21
Ti	0.20	0.21	0.21	0.23	0.25	0.20	0.19	0.19	0.20	0.21	0.22
Fe^{3+}	0.87	0.96	0.88	1.12	1.19	1.29	0.96	1.00	1.02	1.04	0.93
Fe^{2+}	0.81	0.73	0.77	0.67	0.60	0.45	0.67	0.65	0.67	0.72	0.74
Mn	0.04	0.04	0.04	0.04	0.04	0.04	0.04	0.05	0.04	0.05	0.04
Mg	2.88	2.86	2.93	2.58	2.58	2.85	2.89	2.88	2.86	2.70	2.85
Ca	1.73	1.71	1.69	1.72	1.72	1.65	1.70	1.70	1.66	1.71	1.70
Na	0.41	0.40	0.46	0.51	0.54	0.44	0.41	0.41	0.48	0.47	0.43
K	0.08	0.08	0.08	0.08	0.08	0.08	0.07	0.07	0.07	0.08	0.06
Cl	0.01	0.01	0.01	0.01	0.01	0.02	0.01	0.01	0.01	0.01	0.02

Density	2440	2440	2440	2440	2440	2440	2440	2440	2440	2440	2440
Grain	4	5	5	5	6	6	6	7	7	7	1
Core/Rim	Core	Core	Core	Core	Core	Core	Core	Core	Core	Core	Rim
SiO_2	45.4	45.2	45.1	45.2	45.2	44.5	44.4	45.8	45.9	45.0	45.5
TiO_2	2.04	2.34	2.30	2.10	1.93	1.63	1.94	1.83	1.78	1.88	1.81
Al_2O_3	11.1	10.4	10.2	10.2	10.4	10.8	10.8	10.5	10.3	10.8	9.9
FeO	14.2	14.2	14.5	14.3	14.6	14.4	14.4	14.3	14.4	14.9	14.3
MnO	0.30	0.26	0.27	0.31	0.31	0.27	0.31	0.32	0.27	0.33	0.38
MgO	13.1	13.4	13.3	13.4	13.3	13.2	12.8	13.4	13.3	13.0	13.7
CaO	11.3	11.4	11.1	11.2	11.1	11.2	11.1	11.0	11.1	11.1	11.1
Na_2O	1.48	1.69	1.50	1.49	1.47	1.55	1.65	1.60	1.40	1.58	2.20
K_2O	0.38	0.48	0.48	0.48	0.40	0.50	0.49	0.46	0.48	0.45	0.39
Cl	0.04	0.06	0.06	0.06	0.06	0.07	0.06	0.06	0.07	0.05	0.05
Total	99.2	99.4	98.8	98.7	98.7	98.1	98.0	99.3	99.0	99.1	99.3

Table A1 (contd.)

Si	6.44	6.44	6.44	6.47	6.45	6.40	6.42	6.48	6.52	6.41	6.48
Al^{iv}	1.56	1.56	1.56	1.53	1.55	1.60	1.58	1.52	1.48	1.59	1.52
Al^{vi}	0.29	0.18	0.15	0.18	0.19	0.23	0.27	0.23	0.24	0.23	0.14
Ti	0.22	0.25	0.25	0.23	0.21	0.18	0.21	0.19	0.19	0.20	0.19
Fe^{3+}	0.94	0.84	1.02	0.97	1.09	1.04	0.89	1.03	1.02	1.04	0.93
Fe^{2+}	0.75	0.84	0.72	0.74	0.65	0.69	0.85	0.67	0.70	0.74	0.77
Mn	0.04	0.03	0.03	0.04	0.04	0.03	0.04	0.04	0.03	0.04	0.05
Mg	2.77	2.85	2.83	2.85	2.82	2.83	2.75	2.83	2.82	2.75	2.92
Ca	1.71	1.74	1.70	1.72	1.69	1.72	1.73	1.67	1.69	1.70	1.69
Na	0.41	0.47	0.42	0.41	0.41	0.43	0.46	0.44	0.38	0.44	0.61
K	0.07	0.09	0.09	0.09	0.07	0.09	0.09	0.08	0.09	0.08	0.07
Cl	0.01	0.01	0.02	0.01	0.01	0.02	0.02	0.01	0.02	0.01	0.01
Density	2440	2440	2440	2440	2440	2440	2440	2440	2440	2440	2440
Grain	1	1	2	2	3	4	4	4	5	5	5
Core/Rim	Rim	Rim	Rim	Rim	Rim	Rim	Rim	Rim	Rim	Rim	Rim
SiO_2	45.2	44.8	44.9	45.9	43.8	44.1	43.5	46.6	42.1	45.4	44.8
TiO_2	1.86	2.22	1.73	1.73	1.74	1.77	1.69	1.23	2.02	1.83	1.49
Al_2O_3	9.7	10.1	10.9	10.3	11.3	11.7	12.9	9.8	13.8	10.6	11.1
FeO	14.5	14.2	14.9	13.8	14.9	15.0	14.8	13.6	15.6	14.6	16.2
MnO	0.34	0.27	0.35	0.40	0.46	0.42	0.34	0.49	0.40	0.40	0.51
MgO	13.4	13.5	13.2	14.1	13.2	13.1	12.6	13.5	12.1	13.4	13.0
CaO	11.1	11.1	11.0	11.2	11.3	10.9	11.2	11.0	11.0	10.7	10.4
Na_2O	2.30	2.43	2.21	2.11	1.91	1.78	1.87	2.09	1.89	1.66	1.73
K_2O	0.41	0.43	0.39	0.31	0.36	0.34	0.35	0.29	0.37	0.38	0.37
Cl	0.08	0.04	0.06	0.03	0.07	0.04	0.05	0.05	0.04	0.04	0.08
Total	98.9	99.1	99.6	99.8	99.0	99.2	99.2	98.7	99.3	99.0	99.7
Si	6.50	6.42	6.38	6.47	6.26	6.25	6.19	6.65	5.99	6.44	6.30
Al^{iv}	1.50	1.58	1.62	1.53	1.74	1.75	1.81	1.35	2.01	1.56	1.70
Al^{vi}	0.14	0.13	0.20	0.18	0.16	0.21	0.35	0.30	0.30	0.20	0.14
Ti	0.20	0.24	0.19	0.18	0.19	0.19	0.18	0.13	0.22	0.20	0.16
Fe^{3+}	0.81	0.80	1.03	0.96	1.14	1.29	1.11	0.78	1.34	1.19	1.57
Fe^{2+}	0.93	0.91	0.74	0.67	0.64	0.49	0.65	0.84	0.52	0.53	0.34
Mn	0.04	0.03	0.04	0.05	0.06	0.05	0.04	0.06	0.05	0.05	0.06
Mg	2.87	2.89	2.80	2.96	2.82	2.77	2.67	2.88	2.57	2.83	2.73
Ca	1.71	1.71	1.67	1.69	1.74	1.66	1.71	1.68	1.67	1.63	1.57
Na	0.64	0.68	0.61	0.58	0.53	0.49	0.52	0.58	0.52	0.46	0.47
K	0.08	0.08	0.07	0.06	0.07	0.06	0.06	0.05	0.07	0.07	0.07
Cl	0.02	0.01	0.01	0.01	0.02	0.01	0.01	0.01	0.01	0.01	0.02
Density	2440	2440	2440	2440	2440	2440	1950	1950	1950	1950	1950
Grain	6	6	6	7	7	7	1	1	1	2	2
Core/Rim	Rim	Rim	Rim	Rim	Rim	Rim	Core	Core	Core	Core	Core

Table A1 (contd.)

SiO_2	43.5	45.2	45.6	45.2	43.7	45.6	45.8	46.1	46.0	45.8	45.1
TiO_2	2.28	1.95	1.81	1.97	2.02	1.42	1.98	1.80	1.92	1.85	2.21
Al_2O_3	10.5	10.2	9.7	11.0	11.2	10.6	10.2	10.0	10.1	10.2	10.9
FeO	14.8	15.0	14.3	14.4	15.0	15.4	14.8	14.6	14.5	13.9	14.8
MnO	0.36	0.33	0.33	0.32	0.31	0.43	0.36	0.38	0.35	0.27	0.31
MgO	12.7	12.9	13.4	13.4	13.4	13.6	13.3	13.2	13.2	13.7	13.1
CaO	11.2	11.0	11.0	10.7	10.9	10.7	11.1	11.0	10.9	11.1	11.1
Na_2O	1.63	1.51	1.50	1.73	2.09	1.58	1.40	1.35	1.54	1.54	1.55
K_2O	0.48	0.44	0.38	0.37	0.37	0.35	0.41	0.43	0.37	0.42	0.49
Cl	0.07	0.05	0.04	0.05	0.06	0.07	0.06	0.07	0.06	0.04	0.06
Total	97.5	98.6	98.0	99.2	99.1	99.8	99.3	98.9	98.9	98.8	99.6
Si	6.33	6.47	6.54	6.39	6.23	6.40	6.49	6.55	6.54	6.51	6.39
Al^{iv}	1.67	1.53	1.46	1.61	1.77	1.60	1.51	1.45	1.46	1.49	1.61
Al^{vi}	0.14	0.20	0.18	0.23	0.12	0.14	0.20	0.23	0.23	0.21	0.21
Ti	0.25	0.21	0.20	0.21	0.22	0.15	0.21	0.19	0.21	0.20	0.24
Fe^{3+}	0.98	1.04	1.03	1.17	1.23	1.45	1.06	1.04	1.00	1.00	1.06
Fe^{2+}	0.82	0.76	0.69	0.53	0.56	0.36	0.68	0.69	0.73	0.65	0.70
Mn	0.04	0.04	0.04	0.04	0.04	0.05	0.04	0.05	0.04	0.03	0.04
Mg	2.76	2.76	2.87	2.82	2.84	2.85	2.80	2.79	2.79	2.91	2.77
Ca	1.75	1.69	1.68	1.62	1.67	1.61	1.68	1.67	1.66	1.69	1.68
Na	0.46	0.42	0.42	0.47	0.58	0.43	0.38	0.37	0.42	0.43	0.42
K	0.09	0.08	0.07	0.07	0.07	0.06	0.07	0.08	0.07	0.08	0.09
Cl	0.02	0.01	0.01	0.01	0.01	0.02	0.01	0.02	0.02	0.01	0.01
Density	1950	1950	1950	1950	1950	1950	1950	1950	1950	1950	1950
Grain	2	3	3	3	4	4	4	5	5	5	6
Core/Rim	Core	Core	Core	Core	Core	Core	Core	Core	Core	Core	Core
SiO_2	43.6	44.5	44.2	43.7	43.3	43.0	43.2	42.8	42.8	42.9	41.8
TiO_2	1.89	2.17	2.16	2.34	1.92	1.93	1.85	2.45	2.12	2.31	2.00
Al_2O_3	12.2	11.7	11.9	11.8	13.5	13.6	13.6	14.6	15.5	15.6	16.1
FeO	14.7	14.6	14.8	14.6	14.9	15.1	14.8	12.8	12.3	12.4	11.8
MnO	0.24	0.28	0.23	0.22	0.30	0.26	0.25	0.30	0.26	0.19	0.17
MgO	12.5	12.7	12.7	12.5	12.4	12.4	12.4	13.2	13.3	13.1	14.1
CaO	11.0	11.1	11.2	11.1	10.9	10.9	10.9	11.2	11.3	11.0	11.3
Na_2O	1.57	1.52	1.69	1.65	1.90	1.96	1.89	1.80	1.96	2.09	2.20
K_2O	0.44	0.56	0.59	0.53	0.40	0.41	0.41	0.44	0.38	0.37	0.38
Cl	0.04	0.08	0.07	0.08	0.04	0.03	0.03	0.03	0.02	0.01	0.02
Total	98.1	99.2	99.5	98.5	99.6	99.6	99.3	99.7	99.9	99.9	99.8
Si	6.26	6.34	6.30	6.29	6.12	6.09	6.12	6.02	5.98	5.99	5.82
Al^{iv}	1.74	1.66	1.70	1.71	1.88	1.91	1.88	1.98	2.02	2.01	2.18
Al^{vi}	0.32	0.31	0.29	0.28	0.37	0.36	0.39	0.44	0.54	0.56	0.46
Ti	0.20	0.23	0.23	0.25	0.20	0.21	0.20	0.26	0.22	0.24	0.21
Fe^{3+}	1.09	0.97	0.95	0.94	1.21	1.23	1.21	1.07	1.03	1.02	1.24

Table A1 (contd.)

Fe^{2+}	0.67	0.77	0.81	0.82	0.55	0.56	0.54	0.44	0.40	0.42	0.13
Mn	0.03	0.03	0.03	0.03	0.04	0.03	0.03	0.04	0.03	0.02	0.02
Mg	2.68	2.69	2.69	2.69	2.62	2.62	2.63	2.76	2.77	2.73	2.94
Ca	1.70	1.70	1.71	1.72	1.65	1.65	1.65	1.69	1.70	1.65	1.69
Na	0.44	0.42	0.47	0.46	0.52	0.54	0.52	0.49	0.53	0.57	0.59
K	0.08	0.10	0.11	0.10	0.07	0.07	0.07	0.08	0.07	0.07	0.07
Cl	0.01	0.02	0.02	0.02	0.01	0.01	0.01	0.01	0.00	0.00	0.00
Density	1950	1950	1950	1950	1950	1950	1950	1950	1950	1950	1950
Grain	6	7	7	7	1	1	2	2	2	3	3
Core/Rim	Core	Core	Core	Core	Rim	Rim	Rim	Rim	Rim	Rim	Rim
SiO_2	42.1	45.6	45.8	46.1	46.2	45.9	44.3	46.3	46.8	41.3	42.3
TiO_2	1.89	1.78	1.76	1.95	1.53	2.02	1.60	1.54	1.53	1.77	1.93
Al_2O_3	15.9	10.6	10.5	10.4	10.6	10.1	11.6	9.9	9.0	15.0	13.3
FeO	11.7	14.9	14.8	15.1	14.5	14.4	14.5	14.0	13.5	12.9	14.2
MnO	0.15	0.36	0.36	0.37	0.34	0.35	0.38	0.46	0.38	0.15	0.21
MgO	13.9	13.1	13.2	13.1	13.4	13.6	12.8	14.9	14.4	13.3	12.7
CaO	11.4	11.0	11.0	11.0	10.9	11.0	11.0	10.0	10.9	11.2	11.0
Na_2O	2.18	1.54	1.47	1.47	1.37	1.52	1.62	1.57	1.41	1.97	1.75
K_2O	0.38	0.49	0.49	0.46	0.33	0.42	0.34	0.29	0.29	0.35	0.38
Cl	0.02	0.08	0.06	0.09	0.04	0.07	0.04	0.05	0.04	0.02	0.03
Total	99.7	99.4	99.3	100.0	99.3	99.4	98.2	99.0	98.3	97.9	97.7
Si	5.89	6.47	6.48	6.50	6.51	6.49	6.35	6.45	6.64	5.90	6.08
Al^{iv}	2.11	1.53	1.52	1.50	1.49	1.51	1.65	1.55	1.36	2.10	1.92
Al^{vi}	0.52	0.24	0.23	0.23	0.26	0.17	0.31	0.09	0.15	0.42	0.33
Ti	0.20	0.19	0.19	0.21	0.16	0.21	0.17	0.16	0.16	0.19	0.21
Fe^{3+}	1.10	1.07	1.10	1.07	1.17	1.09	1.13	1.63	1.14	1.27	1.22
Fe^{2+}	0.27	0.69	0.66	0.71	0.55	0.61	0.61	0.00	0.47	0.27	0.49
Mn	0.02	0.04	0.04	0.04	0.04	0.04	0.05	0.05	0.05	0.02	0.03
Mg	2.90	2.77	2.79	2.74	2.82	2.86	2.74	3.09	3.04	2.83	2.72
Ca	1.72	1.67	1.67	1.66	1.65	1.66	1.68	1.49	1.65	1.71	1.70
Na	0.59	0.42	0.40	0.40	0.37	0.42	0.45	0.42	0.39	0.54	0.49
K	0.07	0.09	0.09	0.08	0.06	0.08	0.06	0.05	0.05	0.06	0.07
Cl	0.01	0.02	0.02	0.02	0.01	0.02	0.01	0.01	0.01	0.00	0.01
Density	1950	1950	1950	1950	1950	1950	1950	1950	1950	1950	1950
Grain	3	4	4	4	5	5	6	6	7	7	7
Core/Rim	Rim	Rim	Rim	Rim	Rim	Rim	Rim	Rim	Rim	Rim	Rim
SiO_2	41.7	41.2	44.6	45.2	42.5	45.7	42.5	41.8	43.6	46.3	44.3
TiO_2	1.83	1.83	1.52	1.64	2.25	1.84	1.71	2.20	1.69	1.56	1.67
Al_2O_3	13.7	15.4	11.2	11.4	14.5	11.4	15.3	15.6	12.9	10.7	12.1
FeO	13.5	14.9	14.7	14.8	15.2	14.4	11.7	12.1	15.2	14.4	15.5
MnO	0.24	0.28	0.46	0.46	0.36	0.39	0.15	0.15	0.41	0.40	0.38

Table A1 (contd.)

MgO	13.1	11.7	13.2	12.8	11.5	12.8	14.1	13.9	12.5	13.7	12.5
CaO	11.0	11.3	10.5	10.4	10.9	10.7	11.2	11.5	10.6	10.8	11.0
Na_2O	2.14	2.03	1.63	1.56	1.98	1.78	2.07	2.04	1.90	1.66	1.62
K_2O	0.33	0.41	0.35	0.37	0.41	0.38	0.36	0.37	0.28	0.31	0.39
Cl	0.02	0.03	0.06	0.07	0.03	0.08	0.01	0.01	0.02	0.04	0.06
Total	97.6	98.9	98.2	98.7	99.6	99.4	99.1	99.6	99.0	99.8	99.5
Si	6.01	5.89	6.35	6.40	6.04	6.46	5.96	5.86	6.18	6.48	6.27
Al^{iv}	1.99	2.11	1.65	1.60	1.96	1.54	2.04	2.14	1.82	1.52	1.73
Al^{vi}	0.33	0.49	0.23	0.30	0.47	0.36	0.49	0.43	0.32	0.25	0.29
Ti	0.20	0.20	0.16	0.17	0.24	0.20	0.18	0.23	0.18	0.16	0.18
Fe^{3+}	1.23	1.13	1.39	1.29	1.07	1.00	1.19	1.16	1.36	1.19	1.24
Fe^{2+}	0.40	0.65	0.36	0.47	0.73	0.71	0.18	0.26	0.44	0.49	0.60
Mn	0.03	0.03	0.06	0.06	0.04	0.05	0.02	0.02	0.05	0.05	0.05
Mg	2.81	2.50	2.80	2.71	2.45	2.70	2.94	2.90	2.65	2.86	2.64
Ca	1.69	1.73	1.60	1.58	1.66	1.62	1.69	1.73	1.60	1.62	1.66
Na	0.60	0.56	0.45	0.43	0.55	0.49	0.56	0.55	0.52	0.45	0.44
K	0.06	0.07	0.06	0.07	0.07	0.07	0.06	0.07	0.05	0.06	0.07
Cl	0.01	0.01	0.02	0.02	0.01	0.02	0.00	0.00	0.01	0.01	0.01

Table A2: Compositions of plagioclase microlites analyzed by electron microprobe.

Mountain	Density (Kg m^{-3})	SiO_2	$Al2O_3$	CaO	Na_2O	K_2O	Total	An	Ab	Or
BZ	1760	53.4	29.2	12.12	4.23	0.11	99.1	61.2	38.1	0.7
BZ	1760	56.3	28.6	10.59	4.94	0.21	100.7	53.9	44.8	1.2
BZ	1760	53.9	28.4	11.20	4.68	0.15	98.3	56.8	42.3	0.9
BZ	1760	52.9	29.6	12.25	4.22	0.12	99.1	61.5	37.8	0.7
BZ	1760	55.3	28.4	11.87	3.76	0.37	99.7	62.5	35.3	2.3
BZ	1760	55.6	27.7	10.51	4.85	0.24	98.8	54.1	44.5	1.4
BZ	1760	56.7	27.2	10.22	4.93	0.29	99.3	52.8	45.4	1.8
BZ	1760	55.2	27.6	10.42	4.98	0.24	98.4	53.2	45.4	1.4
BZ	1760	56.7	26.6	9.74	5.13	0.39	98.6	50.4	47.2	2.4
BZ	1760	56.2	26.1	9.60	4.99	0.41	97.3	50.6	46.9	2.5
BZ	1950	55.0	28.4	11.12	4.61	0.23	99.3	56.7	41.9	1.4
BZ	1950	54.2	29.3	12.09	4.15	0.16	99.9	61.4	37.6	1.0
BZ	1950	52.8	28.7	12.03	4.13	0.19	97.8	61.3	37.5	1.2
BZ	1950	53.7	28.2	11.32	4.60	0.19	98.0	57.3	41.5	1.1
BZ	1950	56.5	28.5	10.86	4.68	0.25	100.7	55.7	42.8	1.5
BZ	1950	55.8	28.5	11.20	4.53	0.22	100.2	57.4	41.3	1.3
BZ	1950	55.9	27.7	10.75	4.72	0.26	99.3	55.2	43.2	1.6
BZ	1950	58.4	26.4	9.12	5.68	0.34	100.0	46.4	51.6	2.0
BZ	1950	57.2	27.4	10.21	5.03	0.33	100.1	52.2	45.8	2.0
BZ	1950	54.5	29.2	11.93	4.11	0.21	99.9	61.2	37.6	1.2
BZ	2220	53.7	28.7	11.71	4.29	0.26	98.6	59.6	38.9	1.5
BZ	2220	57.3	27.0	9.98	4.85	0.38	99.6	52.3	45.4	2.3
BZ	2220	58.7	26.3	10.10	4.16	0.44	99.7	56.0	41.1	2.8
BZ	2220	54.0	27.9	11.06	4.57	0.29	97.8	56.6	41.7	1.7
BZ	2220	54.7	28.6	11.24	4.41	0.29	99.3	57.8	40.4	1.8
BZ	2220	52.8	30.9	13.37	3.66	0.18	100.9	66.5	32.4	1.1
BZ	2220	53.4	29.5	12.32	4.09	0.14	99.5	62.3	36.9	0.8
BZ	2220	53.3	29.5	12.16	4.15	0.17	99.2	61.6	37.4	1.0
BZ	2220	55.3	28.6	11.10	4.60	0.28	99.9	56.6	41.8	1.6
BZ	2220	54.6	28.5	11.32	4.34	0.28	99.0	58.4	39.9	1.7
BZ	2270	54.0	28.7	11.85	4.24	0.28	99.1	60.1	38.3	1.6
BZ	2270	54.7	27.3	10.66	4.58	0.39	97.6	55.3	42.3	2.4
BZ	2270	55.8	27.8	10.63	4.68	0.44	99.3	54.6	42.8	2.6
BZ	2270	54.1	28.5	11.93	4.10	0.34	99.0	60.7	37.2	2.0
BZ	2270	53.6	29.2	12.30	4.03	0.29	99.4	62.1	36.2	1.7
BZ	2270	56.1	28.2	11.02	4.46	0.44	100.2	56.6	40.8	2.6
BZ	2270	53.9	29.0	12.04	4.06	0.31	99.3	61.3	36.9	1.9
BZ	2270	54.3	28.1	11.32	4.37	0.37	98.5	57.9	39.9	2.2
BZ	2270	53.3	29.3	12.21	3.86	0.31	99.0	62.8	35.4	1.9
BZ	2270	54.4	28.3	11.38	4.37	0.35	98.9	58.2	39.8	2.1
BZ	2270	54.8	28.1	10.98	4.51	0.41	98.8	56.3	41.2	2.5
BZ	2440	53.2	28.8	11.94	4.12	0.34	98.5	60.7	37.3	2.0

Table A2- Contd.

Mountain	Density (Kg m^{-3})	SiO_2	$Al2O_3$	CaO	Na_2O	K_2O	Total	An	Ab	Or
BZ	2440	53.1	29.0	11.96	4.18	0.32	98.6	60.5	37.7	1.9
BZ	2440	54.1	28.0	11.14	4.43	0.43	98.1	57.0	40.4	2.6
BZ	2440	58.8	25.4	9.71	4.44	0.52	98.8	53.3	43.4	3.3
BZ	2440	56.3	27.1	10.47	4.58	0.38	98.8	54.9	42.8	2.3
BZ	2440	53.3	29.1	12.02	4.24	0.29	98.9	60.3	37.9	1.7
BZ	2440	54.0	28.8	11.69	4.25	0.34	99.1	59.4	38.5	2.0
BZ	2440	53.0	29.5	12.33	3.99	0.31	99.1	62.3	35.9	1.8
BZ	2440	54.2	28.8	11.83	4.23	0.32	99.4	59.9	38.2	1.9
BZ	2440	54.7	28.5	11.61	4.27	0.34	99.4	59.2	38.8	2.0
BZ	2560	57.9	26.3	8.80	5.64	0.53	99.2	45.2	51.7	3.1
BZ	2560	58.1	26.0	8.36	5.70	0.56	98.7	43.6	53.0	3.4
BZ	2560	53.4	29.0	11.78	4.20	0.26	98.7	60.2	38.2	1.5
BZ	2560	54.1	29.1	11.84	4.36	0.29	99.7	59.4	38.9	1.7
BZ	2560	55.4	27.8	10.29	4.96	0.39	98.8	52.6	45.1	2.3
BZ	2560	55.6	27.8	10.29	4.97	0.36	99.0	52.6	45.3	2.2
BZ	2560	55.2	28.0	10.71	4.84	0.35	99.2	54.2	43.7	2.0
BZ	2560	60.8	23.7	7.44	5.29	1.03	98.3	41.2	52.2	6.7
BZ	2560	58.2	26.3	9.67	4.73	0.57	99.5	51.5	45.0	3.5
BZ	2560	59.1	25.2	8.23	5.34	0.65	98.5	44.5	51.5	4.1
MSH	1360	60.0	24.6	7.24	6.30	0.36	98.5	38.3	59.4	2.2
MSH	1360	57.5	26.1	8.58	5.85	0.20	98.2	44.6	54.2	1.2
MSH	1360	60.2	24.8	7.43	6.45	0.28	99.2	38.6	59.7	1.7
MSH	1360	60.2	24.8	7.31	6.40	0.29	99.0	38.3	59.9	1.7
MSH	1360	58.6	25.4	7.83	6.28	0.27	98.4	40.5	57.9	1.6
MSH	1360	57.8	26.2	8.61	5.94	0.24	98.8	44.2	54.4	1.4
MSH	1360	58.0	25.6	8.03	6.07	0.22	98.0	42.0	56.6	1.4
MSH	1360	58.2	25.4	7.93	6.26	0.23	98.1	41.0	57.6	1.4
MSH	1360	58.7	25.9	8.33	6.15	0.22	99.2	42.6	56.0	1.3
MSH	1360	57.1	26.1	8.77	5.89	0.21	98.1	45.0	53.8	1.2
MSH	1360	57.4	25.6	8.32	6.09	0.22	97.6	42.8	55.9	1.3
MSH	1360	56.7	26.3	9.08	5.77	0.19	98.1	46.4	52.5	1.1
MSH	1360	57.9	25.5	8.07	6.24	0.26	97.9	41.4	57.0	1.6
MSH	1670	56.4	26.7	9.20	5.66	0.14	98.1	47.3	51.9	0.9
MSH	1670	56.5	26.6	9.14	5.69	0.21	98.1	46.8	52.0	1.2
MSH	1670	61.6	23.1	6.63	6.24	0.31	97.8	36.6	61.4	2.0
MSH	1670	57.3	26.0	8.40	6.02	0.24	97.9	43.3	55.3	1.4
MSH	1670	57.5	25.9	8.37	6.08	0.21	98.1	43.0	55.7	1.3
MSH	1670	58.1	25.5	8.02	6.11	0.24	98.0	41.8	56.8	1.5
MSH	1670	58.4	25.5	7.82	6.30	0.24	98.4	40.5	58.1	1.4
MSH	1670	54.4	28.3	11.02	4.80	0.16	98.7	55.8	43.3	0.9
MSH	1670	57.4	25.9	8.47	6.07	0.19	98.0	43.4	55.4	1.1
MSH	1670	62.0	22.3	5.80	6.32	0.57	97.0	32.7	63.5	3.8
MSH	1670	58.2	25.1	7.66	6.30	0.27	97.5	39.9	58.5	1.6

Table A2 – Contd.

Mountain	Density (Kg m^{-3})	SiO_2	$Al2O_3$	CaO	Na_2O	K_2O	Total	An	Ab	Or
MSH	1670	57.8	25.5	7.94	6.22	0.23	97.7	41.1	57.5	1.4
MSH	1880	64.6	21.5	5.27	6.41	0.57	98.3	30.3	65.8	3.8
MSH	1880	65.1	22.8	6.38	6.20	0.46	100.9	35.5	61.5	3.0
MSH	1880	59.9	25.3	7.84	6.10	0.37	99.5	40.9	56.8	2.2
MSH	1880	63.7	21.7	5.23	5.86	0.79	97.3	31.5	63.0	5.5
MSH	1880	62.6	23.3	6.19	6.38	0.52	99.0	34.1	62.6	3.3
MSH	1880	59.3	25.6	7.97	6.05	0.36	99.2	41.6	56.2	2.2
MSH	1880	64.6	21.5	5.21	6.02	0.53	97.8	31.5	64.8	3.7
MSH	1880	61.1	23.4	6.22	6.50	0.42	97.6	34.0	63.3	2.7
MSH	1880	58.4	25.9	8.20	5.87	0.29	98.7	43.1	55.1	1.8
MSH	1880	58.7	25.0	7.73	5.94	0.34	97.7	41.3	56.6	2.1
MSH	1880	58.5	25.5	8.41	5.68	0.31	98.3	44.5	53.6	1.9
MSH	1880	58.5	26.1	8.34	5.80	0.28	99.0	43.9	54.4	1.7
MSH	1880	57.3	26.3	8.88	5.64	0.27	98.4	46.1	52.2	1.6
MSH	1880	59.3	25.1	7.77	5.96	0.38	98.5	41.2	56.4	2.4
MSH	2250	59.4	25.0	7.74	6.14	0.45	98.7	40.3	57.0	2.7
MSH	2250	57.5	26.5	8.95	5.72	0.28	98.9	46.0	52.4	1.6
MSH	2250	59.4	25.8	8.39	6.01	0.35	99.9	43.0	54.9	2.1
MSH	2250	58.4	25.8	8.39	5.92	0.34	98.8	43.4	54.5	2.1
MSH	2250	57.8	26.3	8.77	5.97	0.31	99.2	44.3	53.8	1.8
MSH	2250	58.3	26.3	8.57	6.06	0.31	99.5	43.4	54.8	1.8
MSH	2250	61.2	24.3	6.97	6.39	0.49	99.4	36.8	60.2	3.0
MSH	2250	58.4	25.8	8.26	6.13	0.34	99.0	42.2	55.8	2.0
MSH	2250	58.3	26.2	8.58	5.96	0.34	99.3	43.8	54.2	2.0
MSH	2250	59.2	25.0	7.62	6.46	0.37	98.6	39.0	58.8	2.2
MSH	2340	65.6	20.5	4.26	6.20	1.38	97.9	25.2	65.4	9.5
MSH	2340	62.8	21.8	3.75	7.38	1.59	97.3	20.0	70.1	9.9
MSH	2340	58.0	26.4	9.32	5.50	0.40	99.6	47.6	50.1	2.4
MSH	2340	62.0	22.3	5.10	6.70	1.32	97.5	27.5	64.3	8.3

Table A3: Glass compositions determined by electron microprobe. Samples are identified by their density

BZ Averages

Density (Kg m-3)	n	SiO_2	TiO_2	Al_2O_3	FeO	MnO	MgO	CaO	Na_2O	K_2O	P_2O_5	Total
1760	11	77.3	0.36	11.1	1.29	0.04	0.14	0.66	3.28	4.02	0.04	98.2
2-s		1.2	0.07	0.3	0.13	0.03	0.04	0.15	0.85	0.13	0.05	
1950	10	78.3	0.35	11.3	1.38	0.04	0.16	0.70	3.20	4.24	0.03	99.7
2-s		0.7	0.06	0.5	0.10	0.03	0.03	0.12	0.52	0.22	0.03	
2220	12	77.0	0.33	11.6	1.30	0.03	0.12	0.72	3.00	4.54	0.04	98.6
2-s		0.9	0.08	0.7	0.25	0.03	0.04	0.33	0.74	0.28	0.04	
2270	3	77.5	0.35	10.9	1.23	0.03	0.30	0.77	2.96	5.09	0.11	99.3
2-s		4.6	0.04	2.0	0.85	0.04	0.66	1.02	0.39	1.78	0.17	
2440	6	77.0	0.39	11.7	1.40	0.05	0.36	0.69	2.63	5.46	0.12	99.8
2-s		1.5	0.10	1.0	0.71	0.05	0.97	0.56	1.42	0.85	0.28	

MSH Averages

Density (Kg m-3)	n	SiO_2	TiO_2	Al_2O_3	FeO	MnO	MgO	CaO	Na_2O	K_2O	P_2O_5	Total
1360	9	77.3	0.35	11.7	1.43	0.02	0.14	0.75	3.37	3.08	0.05	98.2
2-s		3.3	0.07	1.0	0.18	0.04	0.02	0.44	1.28	0.26	0.02	
1670	6	77.6	0.33	11.7	1.27	0.03	0.16	0.79	3.50	3.19	0.13	98.7
2-s		2.8	0.07	0.6	0.13	0.03	0.11	0.47	0.26	0.34	0.21	
1880	7	77.7	0.32	11.9	1.45	0.02	0.16	0.68	3.70	3.77	0.07	99.8
2-s		2.2	0.07	0.9	0.14	0.03	0.06	0.30	0.53	0.20	0.07	
2250	11	77.0	0.42	11.8	1.61	0.03	0.15	0.54	3.64	4.19	0.09	99.4
2-s		1.5	0.08	0.7	0.22	0.05	0.08	0.42	0.70	0.29	0.04	

Individual Analyses

Mountain	Density (Kg/m^3)	SiO_2	TiO_2	Al_2O_3	FeO	MnO	MgO	CaO	Na_2O	K_2O	P_2O_5	Total
BZ	1760	76.1	0.39	11.3	1.37	0.04	0.13	0.69	3.15	3.96	0.02	97.1
BZ	1760	76.2	0.37	11.2	1.19	0.01	0.18	0.87	2.96	4.05	0.08	97.1
BZ	1760	77.2	0.34	11.2	1.37	0.06	0.16	0.70	3.45	4.09	0.03	98.6
BZ	1760	77.4	0.32	11.2	1.32	0.02	0.12	0.66	3.13	4.09	0.02	98.2
BZ	1760	77.4	0.39	11.0	1.19	0.03	0.17	0.64	3.15	4.06	0.07	98.1
BZ	1760	77.4	0.41	11.0	1.20	0.02	0.14	0.62	3.61	4.02	0.01	98.4
BZ	1760	77.4	0.39	11.3	1.29	0.04	0.15	0.61	3.29	3.95	0.06	98.4
BZ	1760	77.4	0.35	11.1	1.31	0.06	0.13	0.65	2.81	3.93	0.06	97.8
BZ	1760	77.6	0.36	11.0	1.30	0.03	0.14	0.68	3.94	4.02	0.05	99.0

Table A3 – Contd.

Mountain	Density (Kg/m^3)	SiO_2	TiO_2	Al_2O_3	FeO	MnO	MgO	CaO	Na_2O	K_2O	P_2O_5	Total
BZ	1760	77.8	0.29	10.9	1.34	0.05	0.14	0.59	2.65	3.93	0.02	97.7
BZ	1760	78.1	0.38	11.4	1.30	0.02	0.13	0.61	3.96	4.07	0.00	100.0
BZ	1950	77.7	0.36	12.0	1.30	0.03	0.14	0.81	3.67	4.03	0.05	100.1
BZ	1950	77.9	0.33	11.4	1.37	0.04	0.16	0.66	2.77	4.19	0.03	98.9
BZ	1950	78.0	0.41	11.2	1.38	0.02	0.15	0.66	3.27	4.13	0.02	99.2
BZ	1950	78.1	0.36	11.2	1.31	0.06	0.14	0.68	3.25	4.31	0.03	99.4
BZ	1950	78.2	0.31	11.4	1.41	0.05	0.17	0.73	3.26	4.34	0.01	99.9
BZ	1950	78.2	0.38	11.2	1.44	0.04	0.15	0.68	3.23	4.22	0.02	99.6
BZ	1950	78.4	0.34	11.5	1.43	0.02	0.17	0.79	3.00	4.22	0.05	99.9
BZ	1950	78.6	0.36	11.2	1.35	0.02	0.16	0.63	3.39	4.39	0.00	100.1
BZ	1950	78.7	0.37	11.2	1.41	0.02	0.16	0.67	2.87	4.36	0.03	99.8
BZ	1950	78.8	0.32	11.2	1.38	0.04	0.16	0.69	3.31	4.24	0.03	100.1
BZ	2220	76.4	0.25	12.0	1.30	0.04	0.09	0.94	3.53	4.35	0.02	98.9
BZ	2220	76.5	0.33	11.1	1.21	0.03	0.11	0.57	2.73	4.52	0.06	97.1
BZ	2220	76.5	0.32	11.5	1.28	0.01	0.12	0.66	2.76	4.71	0.02	97.9
BZ	2220	76.6	0.38	11.5	1.22	0.03	0.13	0.72	3.07	4.57	0.03	98.3
BZ	2220	76.7	0.36	11.0	1.38	0.05	0.12	0.55	2.73	4.65	0.03	97.6
BZ	2220	77.1	0.33	12.4	1.19	0.02	0.11	1.00	2.67	4.50	0.04	99.3
BZ	2220	77.1	0.40	11.4	1.62	0.04	0.17	0.55	2.34	4.64	0.02	98.3
BZ	2220	77.1	0.30	11.9	1.31	0.01	0.14	0.89	3.21	4.52	0.08	99.4
BZ	2220	77.2	0.32	11.4	1.16	0.04	0.13	0.65	2.90	4.54	0.02	98.4
BZ	2220	77.4	0.34	11.5	1.35	0.02	0.14	0.68	3.12	4.50	0.03	99.1
BZ	2220	77.5	0.34	11.4	1.39	0.02	0.11	0.57	3.47	4.69	0.02	99.5
BZ	2220	77.8	0.33	11.6	1.20	0.02	0.11	0.87	3.41	4.23	0.05	99.6
BZ	2270	75.8	0.35	12.1	1.56	0.05	0.67	1.33	3.19	5.32	0.21	100.6
BZ	2270	76.6	0.33	10.6	1.39	0.01	0.17	0.34	2.83	5.83	0.05	98.1
BZ	2270	80.2	0.36	10.2	0.75	0.03	0.05	0.64	2.87	4.10	0.07	99.2
BZ	2440	76.0	0.37	10.8	2.06	0.09	1.33	1.04	2.23	4.82	0.39	99.2
BZ	2440	76.2	0.43	11.9	1.10	0.04	0.08	0.72	4.06	5.17	0.03	99.8
BZ	2440	76.7	0.30	12.4	1.26	0.01	0.09	1.00	2.25	5.44	0.14	99.7
BZ	2440	77.4	0.42	11.8	1.13	0.03	0.29	0.56	2.47	5.75	0.03	99.9
BZ	2440	77.6	0.41	11.6	1.37	0.05	0.23	0.46	2.45	6.04	0.06	100.3
BZ	2440	77.9	0.40	11.5	1.52	0.06	0.13	0.37	2.31	5.53	0.06	99.8
MSH	1360	76.7	0.37	11.6	1.30	0.03	0.15	0.76	3.20	3.08	0.04	97.2
MSH	1360	74.6	0.27	12.4	1.31	0.01	0.13	1.16	4.12	2.96	0.05	97.0
MSH	1360	77.5	0.37	12.6	1.41	0.03	0.13	0.90	4.68	3.00	0.06	100.7
MSH	1360	79.2	0.38	11.4	1.36	0.05	0.15	0.62	3.24	3.17	0.06	99.6
MSH	1360	77.1	0.37	11.1	1.51	0.00	0.14	0.54	2.98	3.30	0.05	97.1
MSH	1360	76.4	0.33	11.5	1.55	0.01	0.16	0.66	3.30	3.15	0.05	97.1
MSH	1360	75.9	0.32	12.1	1.48	0.00	0.12	0.98	3.31	2.93	0.05	97.2
MSH	1360	79.7	0.36	11.4	1.46	0.04	0.15	0.56	2.79	2.96	0.07	99.5

Table A3 – Contd.

Mountain	Density (Kg/m^3)	SiO_2	TiO_2	Al_2O_3	FeO	MnO	MgO	CaO	Na_2O	K_2O	P_2O_5	Total
MSH	1360	78.8	0.38	11.3	1.48	0.01	0.14	0.56	2.70	3.18	0.05	98.6
MSH	1670	78.9	0.32	11.3	1.24	0.03	0.13	0.57	3.73	3.23	0.10	99.5
MSH	1670	77.8	0.36	11.6	1.32	0.03	0.12	0.63	3.49	3.39	0.08	98.8
MSH	1670	75.3	0.36	12.2	1.23	0.02	0.25	1.24	3.57	2.95	0.17	97.3
MSH	1670	77.3	0.32	11.7	1.20	0.05	0.12	0.77	3.44	3.08	0.09	98.1
MSH	1670	77.1	0.29	11.5	1.37	0.01	0.15	0.79	3.35	3.37	0.33	98.2
MSH	1670	79.3	0.30	11.9	1.23	0.03	0.21	0.77	3.43	3.14	0.04	100.3
MSH	1880	76.4	0.33	12.5	1.39	0.04	0.12	0.81	4.24	3.90	0.10	99.8
MSH	1880	76.0	0.27	11.7	1.41	0.02	0.14	0.72	3.80	3.77	0.06	97.9
MSH	1880	78.7	0.36	11.2	1.40	0.03	0.15	0.50	3.42	3.72	0.05	99.5
MSH	1880	77.6	0.32	12.4	1.49	0.01	0.17	0.78	3.66	3.74	0.09	100.3
MSH	1880	78.1	0.29	12.2	1.48	0.02	0.17	0.87	3.68	3.61	0.13	100.5
MSH	1880	78.5	0.30	11.7	1.39	0.01	0.17	0.55	3.56	3.78	0.02	99.9
MSH	1880	78.8	0.35	11.7	1.57	0.04	0.22	0.53	3.54	3.90	0.05	100.7
MSH	2250	76.7	0.41	12.0	1.75	0.05	0.19	0.71	3.83	4.10	0.06	99.8
MSH	2250	75.4	0.35	12.1	1.57	0.04	0.23	0.76	4.16	4.14	0.08	98.8
MSH	2250	76.4	0.48	11.5	1.53	0.04	0.12	0.46	3.64	4.05	0.11	98.3
MSH	2250	77.5	0.39	12.1	1.52	0.00	0.12	0.75	4.18	4.06	0.09	100.7
MSH	2250	78.4	0.44	11.4	1.58	0.01	0.15	0.33	3.22	4.31	0.10	99.9
MSH	2250	76.7	0.39	11.6	1.67	0.06	0.12	0.34	3.16	4.39	0.12	98.5
MSH	2250	77.0	0.41	11.5	1.55	0.02	0.12	0.30	3.37	4.44	0.08	98.8
MSH	2250	77.3	0.46	11.4	1.77	0.06	0.21	0.37	3.40	4.21	0.11	99.3
MSH	2250	76.8	0.48	11.5	1.77	0.00	0.17	0.44	3.47	4.20	0.09	98.9
MSH	2250	77.3	0.41	12.3	1.57	0.01	0.14	0.90	3.91	3.99	0.06	100.7
MSH	2250	76.9	0.42	12.0	1.46	0.00	0.12	0.56	3.70	4.22	0.12	99.6
Anal. Unc.		1.2	0.09	0.3	0.24	0.03	0.05	0.09	0.51	0.30	0.03	

REFERENCES

Adams, N.K., Houghton, B.F. and Hildreth, W. (2006) Abrupt transitions during sustained explosive eruptions: examples from the 1912 eruption of Novarupta, Alaska. Bull Volcanol. 69, 189-206.

Alidibirov, M.A. (1995) A model for viscous magma fragmentation during volcanic blasts. Bull. Volcanol. 56, 459–465.

Alidibirov, M.A. and Dingwell, D.B. (1996) Magma fragmentation by rapid decompression. Nature, 380,146–149.

Alidibirov, M.A., Bogoyavlenskaya, G.E., Kirsanov, I.T., Firstov, P.P., Girina, O.A., Belousov, A.B., Zhdanova, E.Yu. and Malyshev, A.I. (1990a) The 1985 eruption of Bezymiannyi. Volcanol. Seismol.,10, 839–863.

Alidibirov, M.A., Belousov, A.B. and Kravchenko, N.M. (1990b) The directed blast phase of the eruption of Bezymianny volcano in 1985. Volcan. Seismol., 9, 798-811.

Alidibirov, M.A., Dingwell, D.B., Stevenson, R., Hess, K-U, Webb, S.L., Zinke, J. (1997) Physical properties of the Mt. St. Helen´s cryptodome magma. Bull. Volcanol. 59, 103-111.

Al'meev, R.R., Ariskin, A.A., Ozerov, A.Yu. and Kononkova, N.N. (2002) Problems of the Stoichiometry and Thermobarometry of Magmatic Amphiboles: An Example of Hornblende from the Andesites of Bezymyannyi Volcano, Eastern Kamchatka. Geokhim., 8, 803-819.

Andersen, C.A. and Hinthorne, .J.R. (1973) Thermodynamic approach to the quantitative interpretation of sputtered ion mass spectra. Anal. Chem., 45. 1421-1428

Anderson, S.W. and Fink, J.H. (1989) Hydrogen-isotope evidence for extrusion mechanisms of the Mount St Helens lava dome. Nature, 341, 521-523.

Barclay, J., Riley, R. S., and Sparks, R. S. J. (1995) Analytical models for bubble growth during decompression of high viscosity magmas. Bull. Volcanol., 57, 422– 431.

Behrens, H. (1995) Determination of water solubilities in high-viscosity melts: An experimental study on $NaAlSi_3Os$ and $KalSi_3Os$ melts. Eur. J. Mineral., 7: 905-920.

Behrens, H. and Stuke, A. (2003) Quantificantion of H_2O contents in silicate glasses using IR spectroscopy – a calibration based on hydrous glasses analysed by Karl Fischer Titration. Glass Sci. Technol. 76, 176-289.

Belousov, A.B. (1996) Deposits of the 30 March 1956 directed blast at Bezymianny volcano, Kamchtka, Russia. Bull. Volcanol. 57, 649-662.

Belousov, A.B. and Belousova, M.G. (1998) Bezymyanny eruption on March 30, 1956 (Kamchatka): sequence of events and debris-avalanche deposits. Volcan. Seismol., 20, 29-47.

Belousov, A.B. and Bogoyavlenskaya, G.E. (1988) Debris avalanche of the 1956 Bezymianny eruption. Proc. Kagoshima Int. Conf. Volc., 460–462.

Belousov, A.B., Voight, B., Belousova, M., Petukhin, A. (2002) Pyroclastic surges and flows from the 8-10 May 1997 explosive eruption of Bezymianny volcano, Kamchatka, Russia. Bull. Volcanol. 64, 455-471.

Belousov A.B., Voight B. and Belousova M.G. (2007) Directed blasts and blast-currents: a comparison of the Bezymianny 1956, Mount St Helens 1980, and Soufriere Hills, Montserrat 1997 eruptions and deposits. Bull. Volcanol. (published online).

Blower, J.D. (2001) Factors controlling permeability-porosity relationships in magma. Bull. Volcanol., 63, 497-504.
Blundy, J. and Cashman, K.V. (2001) Magma ascent and crystallisation at Mount St. Helens, 1980-1986. Contrib. Mineral. Petr. 140, 631-650.
Bogoyavlenskaya, G.E., and Kirsanov, I.T. (1981) Twenty five years of volcanic activity of Bezymianny. Volcanol. Seismol., 2, 3–13 (in Russian).
Bogoyavlenskaya, G.E., Braitseva, O.A., Melekestsev, I.V., Kirianov, V.Yu., Miller, C.D. (1985) Catastrophic eruptions of the directed blast type at Mount St.Helens, Bezymyanny and Shiveluch volcanoes. J. Geodyn. 3: 189-218.
Braitseva, O.A., Melekestsev, I.V., Bogoyavlenskaya, G.E. and Maksimov, A.P. (1991) Bezymiannyi: eruptive history and dynamics. Volcan. Seismol., 12, 165-195.
Brugger, C.R., Johnston, A.D., Cashman, K.V. (2003) Phase equilibria in silicic systems at one-atmosphere. Contrib. Mineral. Petr. 146:356-369.
Cashman, K.V. (1988) Crystallization of Mount St. Helens 1980-1986 dacite: a quantitative textural approach. Bull. Volcanol., 50, 194-209.
Cashman, K.V. (1992) Groundmass crystallization of Mount St. Helens dacite, 1980-1986: A tool for interpreting shallow magmatic processes. Contrib. Mineral. Petr., 109, 431-449.
Cashman, K.V. (1993) Relationship between crystallization and cooling rate - insight from textural studies of dikes. Contrib. Mineral. Petr., 113,126-142.
Cashman, K.V. and Taggart, J.E. (1983) Petrologic monitoring of 1981-1982 eruptive products from Mount St. Helens, Washington. Science, 221,1385-1387.
Cashman, K.V., Hoblitt, R.P. (2004) Magmatic precursors to the 18 May 1980 eruption of Mount St Helens. Geology 32,141–144.
Chappell, B. (1992) Trace element analysis of rocks by X-ray spectrometry: Adv. X-ray Anal., 34, 263-276.
Christiansen, R.L. and Peterson, D.W. (1981) Chronology of the 1980 eruptive activity. In: Lipman, P.W., Mullineaux, D.R. (Eds.), The 1980 Eruptions of Mount St. Helens, Washington. U.S. Geol. Surv. Prof. Pap. 1250, 17-30.
Costa A., Caricchi L., Bagdassarov N. (2009) A model for the rheology of particle-bearing suspensions and partially molten rocks. Geochem. Geophys. Geosyst., *10*, Q03010.
Crandell, D.R. and Hoblitt, R.P. (1986) Lateral blasts at Mount St. Helens and hazard zonation. Bull. Volcanol., 48:1, 27-37.
Deer, W., Howie, R and Zussman, J. (1992). An Introduction to the Rock-Forming Minerals. Pearson Education Limited publishing. 2nd edition.
DeHoff, R.T. and Rhines, F.N. (1968) Quantitative Microscopy. New York: McGraw-Hill Book Co.
Devine, J.D., Gardner, J.E., Brack, H.P., Layne, G.D., Rutherford, M.J. (1995) Comparison of microanalytical methods for estimating H_2O contents of silicic volcanic glasses. Am. Mineral. 80:3–4, 319–328.
Dingwell, D.B. (1997) The brittle-ductile transition in high-level granitic magmas: Material constraints. J. Petrol. 38:12, 1635-1644.
Dobson, P.F., Epstein, S., Stolper, E.M. (1989) Hydrogen isotope fractionation between coexisting vapo and silicate glasses and melts at low pressure. Geochim. Cosmochim. Acta, 53, 554-572.

Donovan, J. J., Kremser, D. and Fournelle, J. H., 2007. Probe for Windows User's Guide and Reference, Enterprise Edition, 355 p., Probe Software, Inc., Eugene, OR.
Dzurisin, D., Denlinginer, R.P., Rosenbaum, J.G. (1990) Cooling rate and thermal structure determined from progressive magnetization of the dacite dome at Mount St. Helens, Washington. J. Geophys. Res. 95, 2763-2780.
Eichelberger, J.C., Carrigan, C.R., Westrich, H.R., and Price, R.H., 1986, Non-explosive silicic volcanism: Nature 323, p. 598–602.
Eichelberger, J.C. and Hayes, D.B. (1982) Magmatic model for the Mount St. Helens blast of May 18, 1980. J. Geophys. Res., 87, 7727-7738.
Elkins, L.T., and Grove, T.L. (1990) Ternary feldspar experiments and thermodynamic models. Am. Mineral., 75, 544-559.
Fisher, R.V. (1990) Transport and deposition of a pyroclastic surge across an area of high relief: the 18 May 1980 eruption of Mount St. Helens, Washington. Geol. Soc. Am. Bull.,102,1038–1054.
Gardner, C.E., Cashman, K.V. and Neal, C.A. (1998) Tephra-fall deposits from the 1992 eruption of Crater Peak, Alaska: implications of clast textures for eruptive processes. Bull. Volcanol., 59, 537-555.
Gardner, J.E. and Denis, M-H. (2004) Heterogeneous bubble nucleation on Fe-Ti oxide crystals in high-silica rhyolitic melts. Geochim. Cosmochim. Acta, 68:7, 3587-3597.
Gardner, J.E., Hilton, M. and Carroll, M.R. (2000) Bubble growth in highly viscous silicate melts during continuous decompression from high pressure. Geochim. Cosmochim. Acta., 64:8, 1473-1483.
Geschwind, C. and Rutherford, M.J. (1995) Crystallization of microlites during magma ascent: the fluid mechanics of recent eruptions at Mount St. Helens. Bull. Volcanol. 57, 356–370.
Giordano D., Russell, J.K., & Dingwell, D.B. (2008) Viscosity of magmatic liquids: A model. Earth Planet. Sc. Lett. 271, 123-134.
Gorshkov, G.S. (1959) Gigantic eruption of the Bezymianny volcano. Bull. Volcanol. 20, 77–109.
Gorshkov, G.S. (1963) Directed volcanic blasts. Bull. Volcanol. 26, 83-88.
Gorshkov, G.S., and Bogoyavlenskaya, G.E., (1965) Bezymyannyi volcano and peculiarities of it's last eruption (1955–1963). Nauka, Moscow (in Russian).
Goto, Y. and McPhie, J. (1998) Endogenous growth of a Miocene submarine dacite cryptodome, Rebun Island, Hokkaido, Japan. J Volcan. Geoth. Res., 84, 273-286.
Gurioli, L., Houghton, B.F., Cashman, K.V. and Cioni, R. (2005) Complex changes in eruption dynamics and the transition between Plinian and phreatomagmatic activity during the 79 AD eruption of Vesuvius. Bull. Volcanol., 67,144-159.
Hammer, J.E., and Rutherford, M.J. (2002) An experimental study of decompression-induced crystallization in silicic melt. J. Geophys. Res., 107(B1), 8-1 – 8-24
Hammer, J.E., Cashman, K.V. and Voight, B. (2000) Magmatic processes revealed by textural and compositional trends in Merapi dome lavas. J. Volcan. Geoth. Res., 100, 165-192.
Harford, C.L., Sparks, R.S.J., Fallick, A.E. (2003) Degassing at the Soufriere Hills Volcano, Montserrat, recorded in matrix glass compositions. J. Petrol. 44, 1503-1523.
Helz, R.T. (1980) Crystallization history of Kilauea Iki lava lake as seen in drill core recovered in 1967–1979. Bull. Volc., 43:4, 675-701.

Hoblitt, R.P., Miller, C.D. and Vallance, J.W. (1981) Origin and stratigraphy of the deposit produced by the May 18 directed blast. In: Lipman, P.W., Mullineaux, D.R. (Eds.), The 1980 Eruptions of Mount St. Helens, Washington. U.S. Geol. Surv. Prof. Pap. 1250, 401-419.

Hoblitt, R.P. (2000) Was the 18 May 1980 lateral blast at Mt St Helens the product of two explosions? Phil. Trans. Royal. Soc. Lon., 358,1639–1661.

Hoblitt, R.P., and Harmon, R.S. (1993) Bimodal density distribution of cryptodome dacite from the 1980 eruption of Mount St. Helens, Washington, Bull. Volcanol., 55, 421-437.

Hoover, S.R., Cashman, K.V. and Manga, M. (2001) The yield strength of subliquidous basalts – experimental results. J. Volcan. Geoth. Res. 107, 1-18.

Houghton, B.F. and Wilson, C.J.N. (1989) A vesicularity index for pyroclastic deposits. Bull. Volcanol. 51, 451–462.

Hrouda, F., Taborska, S., Schulmann, K., Jezek, J, and Dolejs, D. (1999) Magnetic fabric and rheology of co-mingled magmas in the Nasavrky Plutonic Complex (E Bohemia): implications for intrusive strain regime and emplacement mechanism. Tectonophys., 307, 93-111.

Ishibashi, H., Sato, H. (2007) Viscosity measurements of subliquidus magmas: Alkali olivine basalt from the Higashi-Matsuura district, Southwest Japan, J. Volcan. Geoth. Res. 160, 223-238.

Jarosewich, E. (2002) Smithsonian microbeam standards. J. Res. Nat. Inst. Stand. Technol., 107, 681-685.

Kadik, A.A., Maksimov, A.P. and Ivanov, B.V. (1986) Physico-chemical conditions for crystallization of andesites. Nauka, Moscow,158 pp. (in Russian).

Kato, H. (1999) Karl Fischer reagents technical manual. Japan, Mitsubishi Chemical Corporation, Japan.

Kieffer, S.W. (1981a) Fluid dynamics of the 18 May blast at Mount St. Helens. In: Lipman, P.W., Mullineaux, D.R. (Eds.), The 1980 Eruptions of Mount St. Helens, Washington. U.S. Geol. Surv. Prof. Pap. 1250, 379-401.

Kieffer, S.W. (1981b) Blast dynamics at Mount St. Helens on 18 May 1980. Nature, 291, 568 – 570.

King, P.L., Vennemann, T.W., Holloway, J.R., Hervig, R.L., Lowenstern, J.B. and Forneris, J.F. (2002) Analytical techniques for volatiles: a case study using intermediate (andesitic) glasses. Am. Mineral., 87, 1077-1089.

Klug, C. and Cashman, K.V. (1994) Vesiculation of May 19, 1980 Mount St. Helens magma. Nature, 22, 468-472.

Lange, R.A. and Carmichael, I.S.E. (1990) Thermodynamic properties of silicate liquids with an emphasis on density, thermal expansion and compressibility. Rev. Min., 24, 25-64.

Lavallée, Y., Hess, K-U., Cordonnier, B. and Dingwell, D.B. (2007) Non-Newtonian rheological law for highly crystalline dome lavas. Geol. 35, 843-846.

Leake, B.E. and 21 others (1997) Nomenclature of Amphiboles: Report of the Subcommittee on Amphiboles of the International Mineralogical Association, Comission on New Minerals and Mineral Names, Can. Mineral., 35:1, 219–246.

Leschik, M., Heide, G., Frischat, G.H., Behrens, H., Wiedenbeck, M., Wagner, N., Heide, K., Geißler, H., Reinholz, U. (2004) Determination of H_2O and D_2O contents in rhyolitic glasses. Phys. Chem. Glasses, 45:4, 238-251.

Lipman, P.W., Moore, J.G., Swanson, D.A. (1981a) Bulging of the north flank before the May 18 eruption - geodetic data. In: Lipman, P.W., Mullineaux, D.R. (Eds.), The 1980 Eruptions of Mount St. Helens, Washington. U.S. Geol. Surv. Prof. Pap. 1250, 143–155.

Lipman, P.W. and Mullineaux, D.R. (1981) The 1980 eruptions of Mount St. Helens, Washington. USGS Prof. Pap. 1250, 844 pp.

Lipman, P.W., Norton, D.R., Taggart, J.E., Brandt, E.L. and Engleman, E.E. (1981b) Compositional variations in 1980 magmatic deposits. *In*: Washington, Lipman, P.W. and Mullineaux, D.R. (eds.), The 1980 Eruptions of Mount St. Helens, U.S. Geol. Surv. Prof. Pap. 1250, 631–640.

Martel, C., Bourdier, J.-L., Pichavant, M. and Traineau, H. (2000) Textures, water content and degassing of silicic andesites from recent plinian and dome forming eruptions at Mount Pelée volcano (Martinique, Lesser Antilles arc). J. Volc. Geoth. Res. 96, 191-206.

Massol, H. and Jaupart, C. (2009) Dynamics of magma flow near the vent: Implications for dome eruptions. Earth Planet. Sc. Lett 279, 185-196.

Moore, G., Venneman, T. and Carmichael, I.S.E. (1998) An empirical model for the solubility of H_2O in magmas to 3 kilobars. Am. Mineral. 83: 36-42.

Moore, J.G. and Albee, W.C. (1981) Topographic and structural changes, March-July 1980 – photogrammeteric data. In: Lipman, P.W., Mullineaux, D.R. (Eds.), The 1980 Eruptions of Mount St. Helens, Washington. USGS Prof. Pap. 1250, 123–134.

Moore, J.G., Lipman, P.W., Swanson, D.A. and Alpha, T.R. (1981) Growth of lava domes in the crater, June 1980-January 1981. In: Lipman, P.W., Mullineaux, D.R. (Eds.), The 1980 Eruptions of Mount St. Helens, Washington. USGS Prof. Pap. 1250, 541-547.

Morgan, G.B. VI, and London, D. (1996) Optimizing the electron microprobe analysis of hydrous alkali aluminosilicate glasses: Am. Mineral., 81, 1176–1185.

Nakada, S. and Motomura, Y. (1999) Petrology of the 1991–1995 eruption at Unzen: effusion pulsation and groundmass crystallization. J. Volcan. Geotherm. Res., 89, 173–196.

Navon, O., Chekmir, A. and Lyakhovsky, V. (1998) Bubble growth in highly viscous melts: Theory, experiments, and autoexplosivity of dome lavas, Earth Planet. Sc. Lett, 160, 763-776.

Newman, S. and Lowenstern, J.B. (2002) VolatileCalc: a silicate melt-H_2O-CO_2 solution model written in Visual Basic for Excel. Comp. Geosc. 28:5, 597-604.

Newman, S., Epstein, S. and Stolper, E. (1988) Water, carbon dioxide, and hydrogen isotopes in glasses from the ca. 1340 A.D. eruption of the Mono craters, California: constraints on degassing phenomena and initial volatile content. J. Volc. Geoth. Res., 35, 75–96.

Norrish, K., and Hutton, J. (1977) An accurate X-ray spectrographic method for the analysis of a wide range of geological samples. Geochim. Cosmochim. Acta, 33, 431-441.

Ozerov, A. Yu., Ariskin, A.A., Kyle, P., Bogoyavlenskaya, G.E. and Karpenko, S.F. (1997) Petrological-geochemical model for genetic relationships between basaltic and andesitic magmatism of Klyuchevskoi and Bezymiannyi Volcanoes, Kamchatka. Petrol., 5:6, 614-635.

Pallister, J.S., Thornber, C.R., Cashman, K.V., Clynne, M.A., Lowers, H.A., Brownfield, I.K., Meeker, G.P. Petrology of the 2004-2006 Mount St. Helens lava dome – implications for magmatic plumbing, explosivity and eruption triggering. *In* Sherrod, D.R., Scott, W.E., and Stauffer, P.H. (eds.), A Volcano Rekindled: The Renewed Eruption of Mount St. Helens, 2004-2006. U.S. Geol. Surv. Prof. Pap. 1750, 648-702.

Pineau F., Semet M.P., Grassioneau N., Okrugin V.M., and Javoy M. (1999) The genesis of the stable isotope (O, H) record in arc magmas: the Kamchatka's case. Chem. Geol. 135, 93–124.

Petford, N. (2003) Rheology of granitic magmas during ascent and emplacement. Ann. Rev. Earth Plan. Sci., 31, 399–427.

Plechov, P. Yu, Tsai, A. E., Shcherbakov, V. D., and Dirksen, O. V. (2008) Opacitization Conditions of Hornblende in Bezymyannyi Volcano Andesites (March 30, 1956 Eruption). Petrol., Vol. 16, No. 1, pp. 19–35.

Proussevitch, A. A. and Sahagian, D. (1998) Dynamics and energetics of bubble growth in magmas: Analytical formulation and numerical modeling. J. Geophys. Res., 103, 18223–18251.

Ritchie, L., Cole, P., Sparks, R.S.J. (2002) Sedimentology of pyroclstic density current deposits generated by the December 26, 1997 eruption at the Soufrière Hills volcano, Montserrat. In: Druitt T., Kokelaar B.P. (eds). The eruption of Soufrière Hills volcano, Montserrat, from 1995-1999. Mem. Geol. Soc. London, 21, 435-456.

Rutherford, M.J., and Hill, P.M. (1993) Magma ascent rates from amphibole breakdown: An experimental study applied to the 1980-86 Mount St. Helens eruptions. J. Geo. Res. 98, 19667-19686.

Rutherford, M.J., Sigurdsson, H., Carey, S.N., and Davis, A.J. (1985) The May 18, 1980 eruption of Mount St. Helens 1. Melt composition and experimental phase equilibria. J. Volc. Geoth. Res. 90: 2929-2947

Schneider, D.J., Vallance, J.W., Wessels, R., Logan, M., and Ramsey, M.S. (2008) Use of thermal infrared imaging for monitoring renewed dome growth at Mount St. Helens. *In* Sherrod, D.R., Scott, W.E., and Stauffer, P.H. (eds.), A Volcano Rekindled: The Renewed Eruption of Mount St. Helens, 2004-2006. U.S. Geol. Surv. Prof. Pap. 1750, 347-359.

Scott, W.E., Sherrod, D.R. and Gardner, C.A. (2008) Overview of the 2004-2006, and continuing, eruption of Mount St. Helens, Washington. In: Sherrod, D.R., Scott, W.E. and Stauffer, P.H. (Eds.), A volcano rekindled: the renewed eruption of Mount St. Helens, 2004-2006. USGS Prof. Pap. 1750, 3-26.

Self, S., and King, A.J. (1996) Petrology and sulfur and chlorine emissions of the 1963 eruption of Gunung Agung, Bali, Indonesia. Bull. Volcanol., 58, 263-285.

Sharp, Z. D., Atudorei, V., and Durakiewicz, T. (2001). A rapid method for determining the hydrogen and oxygen isotope ratios from water and solid hydrous substances. Chem. Geol. 178, 197–210.

Siebert, L., Beget, J.E. and Glicken, H.X. (1995) The 1883 and late-prehistoric eruptions of Augustine volcano, Alaska. J. Volcan. Geoth. Res., 66, 367–395.

Silver, L.A., Ihinger, P.D., and Stolper, E. (1990) The influence of bulk composition on the speciation of water in silicate glasses. Contrib. Mineral. Petr.,104, 142–162.
Spieler, O., Kennedy, B., Kueppers, U., Dingwell, D.B., Scheu, B. and Taddeucci, J. (2004) The fragmentation threshold of pyroclastic rocks. Earth Planet. Sci. Lett., 226:1-2, 139-148.
Stevenson, R.J., Dingwell, D.B., Webb, S.L., and Sharp, T.G. (1996) Viscosity of microlite-bearing rhyolitic obsidians: An experimental study. Bull. Volcanol., 58, 298–309.
Stewart, A.L. and McPhie, J. (2003) Internal structure and emplacement of an Upper Pliocene dacite cryptodome, Milos Island, Greece. J. Volcan. Geoth. Res., 124, 129-148.
Takeuchi, S., Nakashima, S., Tomiya, A. and Shinohara, H. (2005) Experimental constraints on the low gas permeability of vesicular magma during decompression. Geophys. Res. Lett., 32, L10312.
Taylor, B.E. (1986) Magmatic volatiles: isotopic variation of C, H and S. Rev. Min. Geoch. 16:1, 185-225.
Taylor, B.E., Eichelberger, J.C. and Westrich, H.R. (1983) Hydrogen isotopic evidence of rhyolitic magma degassing during shallow intrusion and eruption. Nature 306, 541–545.
Thomas, N., Jaupart, C., and Vergniolle, S. (1994) On the vesicularity of pumice. J. Geophy. Res., 99, 15633–15644.
Tindle, A.G., and Webb, P.C. (1994) PROBE-AMPH—a spreadsheet program to classify microprobe-derived amphibole analyses. Comp. Geosc., 20:7-8, pp. 1201–1228.
Toramaru, A. (1995) Numerical study of nucleation and growth of bubbles in viscous magmas. J. Geophys. Res., 100, 1913–1931.
Tuttle, O.F. and Bowen, N.L. (1958) Origin of granite in the light of experimental studies in the system $NaAlSi_3O_8$-$KAlSi_3O_8$-SiO_2-H_2O. Geo. Soc. Am. Mem. 74, 151 pp.
van der Plas, L., and Tobi, A. C., (1965) A chart for judging the reliability of point counting results. American Journal of Science, 263: 87-90.
Vennemann, T.W. and O'Neil, J.R. (1993). A simple and inexpensive method of hydrogen isotope and water analyses of minerals and rocks based on zinc reagent. Chem. Geol. 103: 227-234.
Vigneresse, J.L., and Tikoff, B. (1999) Strain partitioning during partial melting and crystallizing felsic magmas: Tectonoph., 312, 117–132.
Vigneresse, J.L., Barbey, P., and Cuney, M. (1996), Rheological transitions during partial melting and crystallization with application to felsic magma segregation and transfer. J. Petrol., 37:6, 1579–1600.
Voight, B. and Elsworth, D. (2000) Instability and collapse of hazardous gas-pressurized lava domes, Geophys. Res. Lett., 27, 1–4.
Voight, B., Glicken, H.X., Janda, R.J. and Douglas, P.M. (1981) Catastrophic rockslide avalanche of May 18. In: Lipman, P.W., Mullineaux, D.R. (Eds.), The 1980 Eruptions of Mount St. Helens, Washington. U.S. Geol. Surv. Prof. Pap. 1250, 347-378.
Wen, S. and Nekvasil, H. (1994) SOLVCALC computer program for feldspar thermometry. Comput. Geosci., 20,1025-1040.
Westrich, H. R. (1987) Determination of water in volcanic glasses by Karl-Fischer titration. Chem. Geol., 163: 335-340.

Wickham, S.M. (1987) The segregation and emplacement of granitic magmas. J. Geol. Soc. London, 144, 281–97.
Wright, T.L. and Okamura, R.T. (1977). Cooling and crystallization of tholeiitic basalt, 1965 Makaopuhi Lava Lake, Hawaii. U.S. Geol. Surv. Prof. Pap. 1004, 78 pp.
Yu, A.B. and Standish, N. (1993) A study of the packing of particles with a mixture size distribution. Powd. Technol. 76, 113-124.

Bezymianny Volcano
14 July 2008